Bulk Nanostructured Materials

C. C. Koch[1*], T. G. Langdon[2,3], E. J. Lavernia[4]

1. Department of Materials Science and Engineering, North Carolina State University, Raleigh, NC 27695, USA

2. Departments of Aerospace & Mechanical Engineering and Materials Science, University of Southern California, Los Angeles, CA 90089, USA

3. Materials Research Group, Faculty of Engineering and the Environment, University of Southampton, SO17 1BJ, UK

4. Department of Chemical Engineering and Materials Science, University of California, Irvine, Irvine, CA 92697, USA

*Corresponding author: email: carl_koch@ncsu.edu

Abstract

This paper will address three topics of importance to bulk nanostructured materials. Bulk nanostructured materials are defined as bulk solids with nanoscale or partly nanoscale microstructures. This category of nanostructured materials has historical roots going back many decades but has relatively recent focus due to new discoveries of unique properties of some nanoscale materials. Bulk nanostructured materials are prepared by a variety of severe plastic deformation methods, and these will be reviewed. Powder processing to prepare bulk nanostructured materials requires that the powders be consolidated by typically combinations of pressure and temperature, the latter leading to coarsening of the microstructure. The thermal stability of nanostructured materials will also be discussed. An example of bringing nanostructured materials to applications as structural materials will be described in terms of the cryomilling of powders and their consolidation.

I. INTRODUCTION

Bulk nanostructured materials are defined as bulk solids with nanoscale or partly nanoscale microstructures. This category of nanostructured materials has historical roots going back many decades but has relatively recent focus due to new discoveries of unique properties of some nanoscale materials.

Early in the last century, when "microstructures" were revealed primarily with the optical microscope, it was recognized that refined microstructures, for example, small grain sizes, often provided attractive properties such as increased strength and toughness in structural materials. A classic example of property enhancement due to a refined microstructure- with features too small to resolve with the optical microscope- was age hardening of aluminum alloys.

The field of nanocrystalline (or nanostructured) materials as a major identifiable activity in modern materials science results to a large degree from the work in the 1980s of Gleiter and co-workers [1] who synthesized nanoscale (<100 nm) grain size materials by the *in situ* consolidation of nanoscale atomic clusters. These nanostructured materials exhibited dramatically improved – or different - properties from conventional grain size (> 1 μm) polycrystalline or single crystal materials of the same chemical composition. This is the stimulus for the tremendous appeal of these materials.

There are a number of processing methods to produce bulk nanostructured materials. These include the inert gas condensation method pioneered by Gleiter [1], electrodeposition [2], crystallization of amorphous precursors [3], severe plastic deformation methods [4], or the consolidation of nanoscale powder precursors [5]. The nanoscale powder precursors may be nanoscale powders produced by a variety of chemical methods [6] or powders which are micron

or tens of microns in size but with a nanoscale grain size produced by ball milling of powders. The methods to be emphasized in this short review will be those that involve either severe plastic deformation of bulk materials, or the severe plastic deformation (mechanical attrition) of powders followed by consolidation into bulk.

The paper will begin with a review of severe plastic deformation techniques. This will be followed by a consideration of the problem of the stabilization of nanoscale grain size in powders during their consolidation which involves elevated temperatures. The concluding section will give an example of aluminum alloys prepared by mechanical alloying and consolidated by conventional commercial processing such as extrusion. Their grain size is stabilized by nanoscale precipitates of oxides and nitrides. A summary will discuss the existing or potential applications of bulk nanostructured materials.

II. BULK NANOSTRUCTURED MATERIALS BY SEVERE PLASTIC DEFORMATION

Metal processing is generally based on conventional procedures, such as rolling, extrusion and drawing, in which one of the dimensions of the work-piece is significantly reduced during the processing operation. Nevertheless, alternative procedures are now available where exceptionally high strains may be imposed without incurring any major changes in the overall dimensions of the samples. This type of processing relates to the application of severe plastic deformation (SPD) and the processing has been defined formally as “any method of metal forming under an extensive hydrostatic pressure that may be used to impose a very high strain on a bulk solid without the introduction of any significant change in the overall dimensions of the sample” [7]. In practice, SPD processing provides a unique opportunity for achieving

exceptional grain refinement, typically to the sub-micrometer or even the nanometer level, and thereby it provides the potential for obtaining superior properties that cannot be achieved using more conventional techniques.

The following section provides a brief historical review of the development of SPD processing leading up to the recognition that these procedures may be used to produce exceptionally small grain sizes in metals and the following sections describe the more recent developments of these procedures and the potential for attaining unusual and useful properties in bulk metallic solids.

A. The Development of SPD as a Processing Tool

SPD processing is generally considered a very new metallurgical tool but in fact comprehensive analyses have shown that the general principles of SPD were employed over 2000 years ago in ancient China [8, 9]. Thus, in the Han dynasty in China around 200 BC a new and effective forging technique was developed for the fabrication of steel for use in swords. This technique consisted of repetitively forging and folding a metal to produce very high strength as in the famous Bai-Lian steels and later a similar technique was used in the processing ultrahigh carbon Wootz steels in ancient India [10] and then Damascus steels in the Middle East [11]. Despite the remarkable success of this approach in achieving high strengths, these procedures were followed by medieval artisans without any formal understanding of the fundamental scientific principles associated with the processing.

The first scientific approach to SPD processing may be traced to the work of P.W. Bridgman at Harvard University dating from the 1930's onwards [12]. Bridgman single-handedly investigated the processing of metals using a combination of compression and torsional straining and thus he essentially introduced the procedure that is known today as High-Pressure Torsion (HPT). Subsequently, in 1946, Bridgman received the Nobel Prize in Physics for his work on

98 the effects of high pressures on bulk metals. Over a period of many years, Bridgman amassed a
99 large volume of data on the applications of high pressures to a remarkably wide range of
100 materials and this work was summarized in a book published in 1952 [13] and more recently in a
101 comprehensive review article [14]. Following Bridgman, the principles of HPT were further
102 developed extensively by scientists working in the Soviet Union [15]. A second important
103 development occurred, also in the Soviet Union, when Segal and co-workers [16] processed
104 metals using the procedure that is now known as Equal-Channel Angular Pressing (ECAP).
105 Nevertheless, all of this work on HPT and ECAP was devoted exclusively to examining the
106 experimental parameters associated with the development of these techniques in the production
107 of high-strength materials and there was no reference to the underlying microstructure that is
108 now recognized to play a major role in determining the fundamental physical properties of the
109 material.

110 In practice, the evolution of SPD processing through microstructural analysis required the
111 introduction of sophisticated analytical tools such as high-resolution transmission electron
112 microscopy and, more recently, electron backscatter diffraction. The first recognition of the
113 importance of these microstructural effects again occurred in the Soviet Union with the work of
114 Valiev and his colleagues in the late 1980's [17]. These investigations provided the first
115 demonstration that it was possible to achieve remarkable grain refinement in many metallic
116 alloys through the use of SPD processing. For example, a grain size of ~0.3 μm was reported in
117 a superplastic Al-4% Cu-0.5% Zr alloy [17] even though in western countries at this time the
118 smallest attainable grain size in this alloy was generally considered to be about ~3-5 μm [18].
119 Later detailed reports of this work in the western literature [19, 20] provided the impetus for the

subsequent rapid expansion of these SPD processing techniques to many laboratories around the world.

In addition to ECAP and HPT, several other SPD procedures have been developed which may be used effectively to process metals without incurring any changes in the overall dimensions and providing the potential for achieving excellent grain refinement. Examples of these methods include accumulative roll bonding (ARB) [21.22], multi-directional forging [23,24], multi-axial compression(MAC) [25,26], cyclic extrusion and compression [27,28], repetitive corrugation and straightening (RCS) [29,30] and twist extrusion [31,32]. Nevertheless, ECAP and HPT are the two SPD procedures used most frequently in modern processing [33] primarily because ECAP is simple to conduct in any laboratory and may be used to provide reasonably large samples and HPT leads to an optimum refined microstructure. For example, in comparisons between HPT and ECAP it was shown that HPT produces smaller grains [34, 35] and a larger fraction of grain boundaries having high angles of misorientation [36]. The superiority of HPT in producing exceptional grain refinement was also demonstrated in direct comparisons with the alternative procedures of MAC [37] and RCS [38].

B. Characteristics of Bulk Nanostructured Materials Produced Using Conventional SPD

Processing by ECAP is a procedure where a sample, in the form of a bar or rod, is pressed through a die constrained within a channel which is bent through an abrupt angle within the die [39]. It has been shown that the strain imposed in a single pass in ECAP is dependent primarily upon the angle subtended internally by the channel and also to a minor extent by the outer arc of curvature where the two parts of the channel intersect. Thus, for a channel angle of 90° and a typical outer arc of curvature of ~20° the imposed strain is close to ~1 on each pass [40]. Repetitive pressings may be undertaken to impose even higher strains and then the orientations

of the samples in each pass become critical because these orientations affect the slip systems within the specimen. For optimum conditions, samples in ECAP are generally processed using route B_C in which the billet is rotated in the same sense by 90° about the longitudinal axis between each pass [41].

Numerous reports are now available documenting the microstructures that may be achieved using ECAP [42,43] but a comprehensive evaluation was presented where high purity (99.99%) aluminum was processed by ECAP at room temperature (RT) for up to 12 passes using a 90° die and then the samples were examined using orientation imagining microscopy (OIM) [44]. The results are shown in Fig. 1 where the grain colors relate to the orientation of each grain as shown in the unit triangle. In these images, high-angle grain boundaries (HAGBs) are defined as boundaries having misorientations of more than 15° and low-angle grain boundaries (LAGBs) have misorientations between 2° and 15°. Fig. 1(a) shows the initial unprocessed microstructure where the grain size was ~1 μm and Figs. 1(b)–(g) show the microstructures after processing by ECAP at RT through 1 to 12 passes: it is important to note that (c)-(f) have similar magnifications but a higher magnification is used in Fig. 1(g) to show more fully the final grain structure. Inspection of these images shows that the grain structure evolves from elongated subgrains to reasonably equiaxed ultrafine grains over 1 to 4 passes and thereafter the average grain size and the grain aspect ratio remain reasonably constant up to 12 passes with a final grain size of ~1.2 μm. Measurements of the boundary misorientations showed the HAGBs accounted for ~74% of all boundaries after 12 passes and there was an increasingly weaker texture after processing through higher numbers of passes. Hardness measurements taken after ECAP processing have demonstrated that there is a high degree of homogeneity in these measurements both on cross-sectional planes [45] and longitudinal planes [46] although there generally remains

a very narrow region of lower hardness, having a width of ~0.5 mm, adjacent to the lower surface. Thus, processing by ECAP is an excellent procedure for achieving very significant grain refinement and a very high degree of microstructural homogeneity. Furthermore, although the results in Fig. 1 relate to high-purity Al where the minimum grain size is ~1.2 μm, very similar results were reported also in an Al-1% Mg solid solution alloy where the minimum grain size was ~700 nm [47].

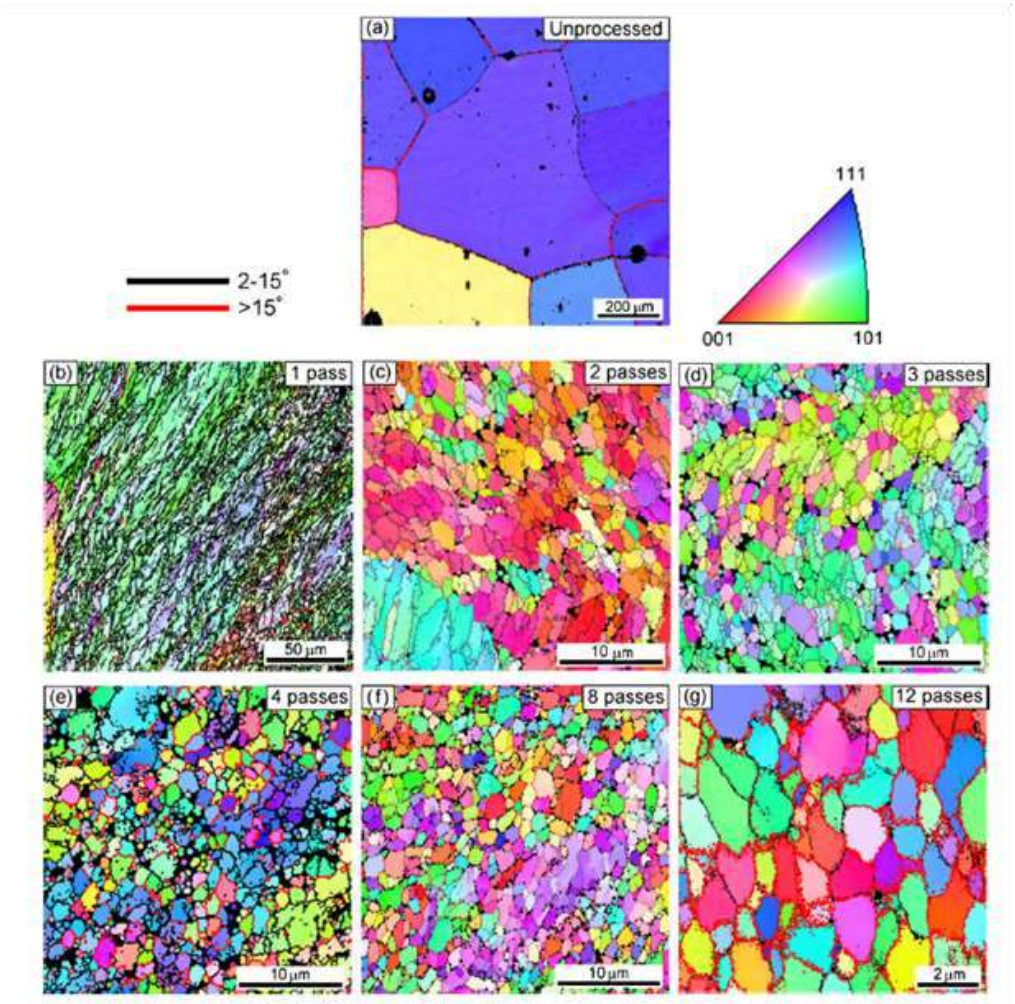

Figure 1 OIM images for high purity aluminum in (a) the initial unprocessed condition and after ECAP through (b) 1, (c) 2, (d) 3, (e) 4, (f) 8 and (g) 12 passes using route BC at RT: the grain colors correspond to the orientations in the unit triangle. Reprinted with permission from reference [44].

178 Processing by HPT is very different from ECAP because it generally uses a sample in the
179 form of a thin disk which is placed between two large anvils and subjected to a high applied
180 pressure and concurrent torsional straining [48]. Furthermore, processing by HPT leads to an
181 equivalent von Mises strain imposed on the disk, ε_{eq}, which is given by a relationship of the
182 form [49,50]:

183 $$\varepsilon_{eq} = \frac{2\pi N r}{h\sqrt{3}} \quad (1)$$

184 where r and h are the radius and height (or thickness) of the disk, respectively and N represents
185 the number of HPT turns. Inspection of Eq. (1) shows that the imposed strain varies across the
186 disk with a maximum value at the outer edge and a strain equal to zero where $r = 0$ at the center
187 of the disk. Thus, it is reasonable to anticipate that the microstructure and measurements of the
188 microhardness will vary significantly across the HPT disk and this suggests that it may be
189 impossible to achieve a high degree of homogeneity. In practice, however, early +experiments
190 showed that it was both possible to achieve a reasonable level of homogeneity after a sufficiently
191 large number of turns [51] and also that the degree of inhomogeneity in HPT disks decreases
192 with increasing strain [52]. It was demonstrated by theoretical analysis that the development of
193 homogeneity may be anticipated based on an application of strain gradient plasticity modeling
194 [53] and detailed experiments showed that excellent hardness homogeneity may be achieved
195 throughout the disks at high strains by measuring the hardness values on sectional planes after
196 straining [54]. The evolution towards a saturation microstructure at high strains may occur in
197 different ways depending upon the extent of any recovery and the precise role of strengthening
198 and weakening [55]. This evolution was examined in a recent comprehensive review which
199 summarizes HPT data for a large number of materials [56].

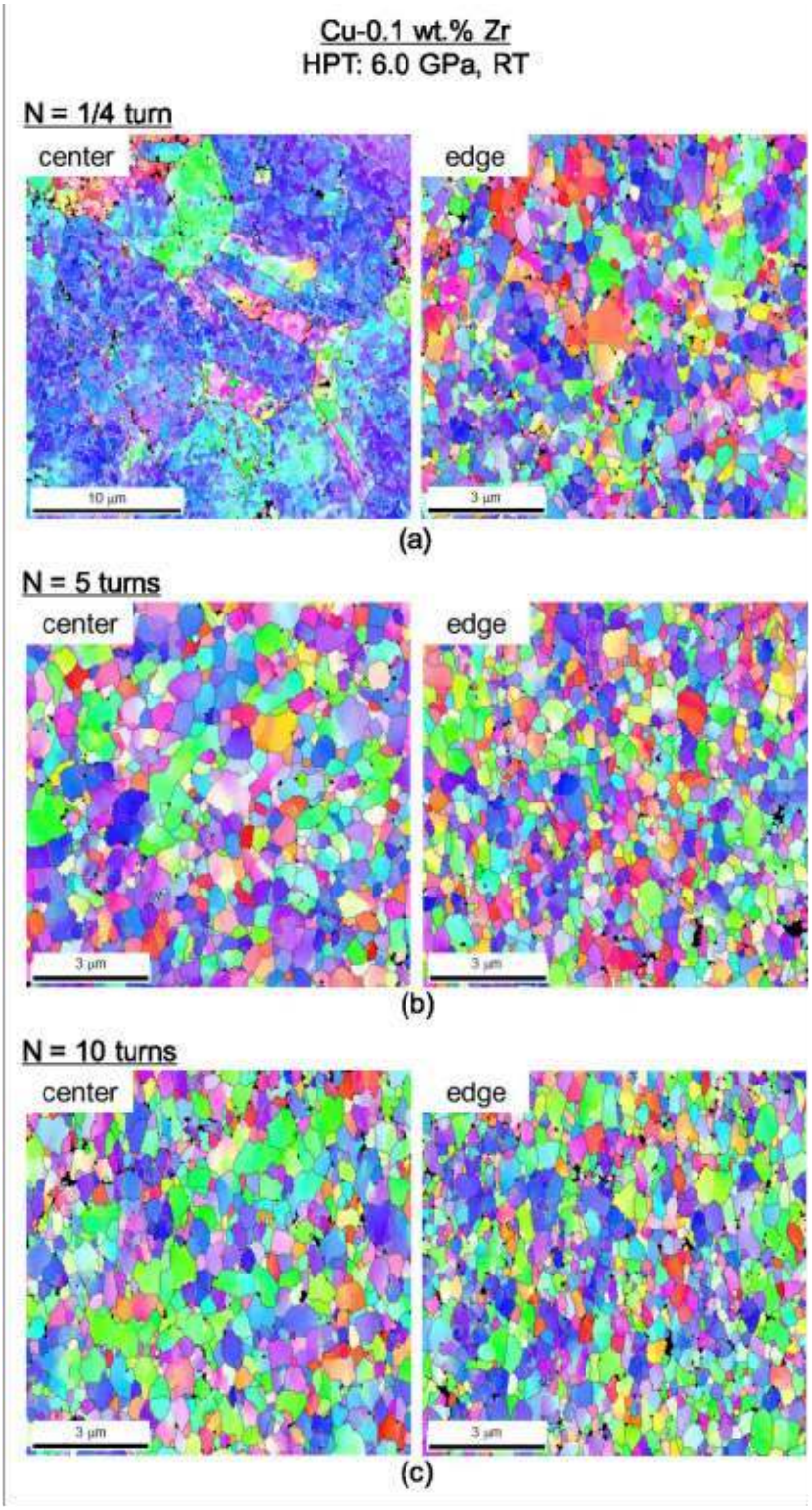

Figure 2. EBSD orientation images of Cu-0.1% Zr disks processed by HPT for (a) 1/4 turn, (b) 5 turns and (c) 10 turns: the columns display images from the center of the disk (on left) and at the edge of the disk (on right). Reprinted with permission from reference [57].

Figure 2 shows electron backscatter diffraction (EBSD) images of the microstructural evolution in a Cu-0.1% Zr alloy processed by HPT at RT under an applied pressure of 6.0 GPa where the three rows relate to 1/4 , 5 and 10 turns and the two columns correspond to the approximate center of the disk on the left and near the edge of the disk on the right, respectively [57]. The grain size initially was ~20 μm but the images show the occurrence of very extensive grain refinement during HPT processing such that after 10 turns the measured grain sizes were ~270 and ~230 nm at the center and near the edge, respectively.

C. Recent Developments in Processing by ECAP

Processing by ECAP can be achieved easily in the laboratory but it is a labor-intensive process because of the need to press the same billet through the die a number of times. Accordingly, much attention has been devoted to developing other approaches that may have more use in industrial applications [58-60]. A simple procedure to avoid the need for multiple pressings in ECAP is to construct a multi-pass die in which a high strain is imposed in a single pass [61]. This procedure works well and produces results which are essentially identical to those achieved using a series of separate passes through a conventional ECAP die [61] but nevertheless it has the disadvantage that it exposes the die to large loads which require special technical solutions. A second problem in conventional ECAP is that is produces billets having gross distortions at either end and this leads to a wastage of material of an estimated order of ~30-50% [62]. In practice, this wastage may be avoided by using an ECAP die having two parallel channels since the second channel restores the original shape of the billet and effectively eliminates the end effects [62]. Accordingly, this approach has been used successfully in several investigations [63-65].

The most effective procedure for improving on conventional ECAP, and for producing long samples with lengths of up to >1 m, is to combine ECAP with the Conform process which was developed over forty years ago in the atomic energy industry in the U.K. [66,67]. Basically, the Conform process permits the continuous extrusion forming of wires using the frictional forces between a wire introduced from a continuous roll and a grove machined into a rotating wheel. This leads to a transition from an initial circular cross-section of the wire to a rectangular cross-section and, by inserting an ECAP step in the form of an abrupt abutment which displaces the wire through 90° at the exit channel, it is feasible to impose a strain of ~1 as in conventional ECAP and to achieve significant grain refinement. Furthermore, unlike conventional ECAP, the ECAP-Conform process may be used in the production of long rods which cannot be processed using conventional ECAP dies. This ECAP-Conform process has been used successfully on several different metals [68-75] and it is illustrated schematically in Fig. 3 [72]. An example of the grain refinement achieved using this procedure is given by results on an Al-6061 alloy where an initial equiaxed grain size of ~350 μm was reduced to elongated grains with lengths of 1.5 μm and widths of ~700 nm after a single pass through the ECAP-Conform die and to lengths of ~1.2 μm and widths of ~150 nm after 4 passes [72].

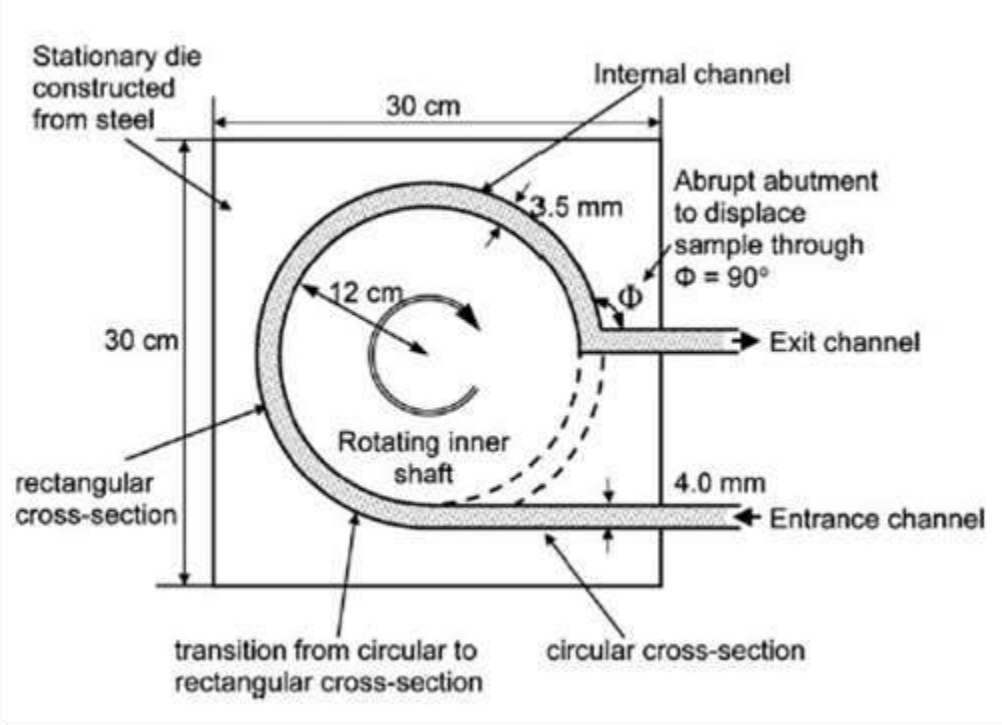

Figure 3. Schematic illustration of the principle of the ECAP–Conform process. Reprinted with permission from reference [72].

D. Producing Gradient Structures and Multi-layered Laminates through Tube Shearing

Multi-layered laminates may be fabricated by ARB when two dissimilar metal sheets are stacked and then subjected to conventional roll bonding. But this procedure requires many cleanings of the metal surfaces and multiple passes through ARB processing so that it is labor-intensive. An alternative approach is to use the process of tube high-pressure shearing (t-HPS) [76]. This latter procedure is based in part on the very early work of Bridgman [77] where tube twisting was introduced as a method of avoiding the problems associated with a lack of strain at the centers of the solid disks. However, the very early work was different because it was based on using a tube sample and then twisting the top with respect to the bottom whereas in t-HPS the sample is again in the form of a tube but the outer surface is sheared around the inner surface by

placing the tube around a central mandrel, using pressure rings to hold the tube in place and produce high hydrostatic pressures in the tube walls, and then using an outer cylinder to rotate the outer surface with respect to the inner surface.

Several experiments have been conducted using t-HPS and the results are encouraging [78]. It was shown that, by using two different metals of an AB-type or with four initial interfaces of an ABAB-type, it can be predicted theoretically that there should be a gradient distribution of interfaces with denser stacking at the inner surface of the tube. This is consistent with experiments and there are numerous other predictions based on different sets of initial interfaces [78]. An important result from this work is that t-HPS can be used with an ABAB-type bimetallic tube to produce a multilayered structure. An example is shown in Fig. 4 where the two materials are 5N and 4N Al which were cut to give four interfaces with an ABAB-type initial structure and then the tube was processed by 2 turns to give a very fine grain size (<1 μm) in the 4N Al and a much coarser grain size (~10 μm) in the 5N Al due to the easier grain growth. It is clear from Fig. 4 that the microstructures of each separate component are very well defined and accordingly the results show that this is an excellent procedure for producing a gradient structure [78]. Furthermore, this result is important because of the current considerable interest both in developing and using gradient structures [79-81] and in the fabrication of nano-laminated structures [82].

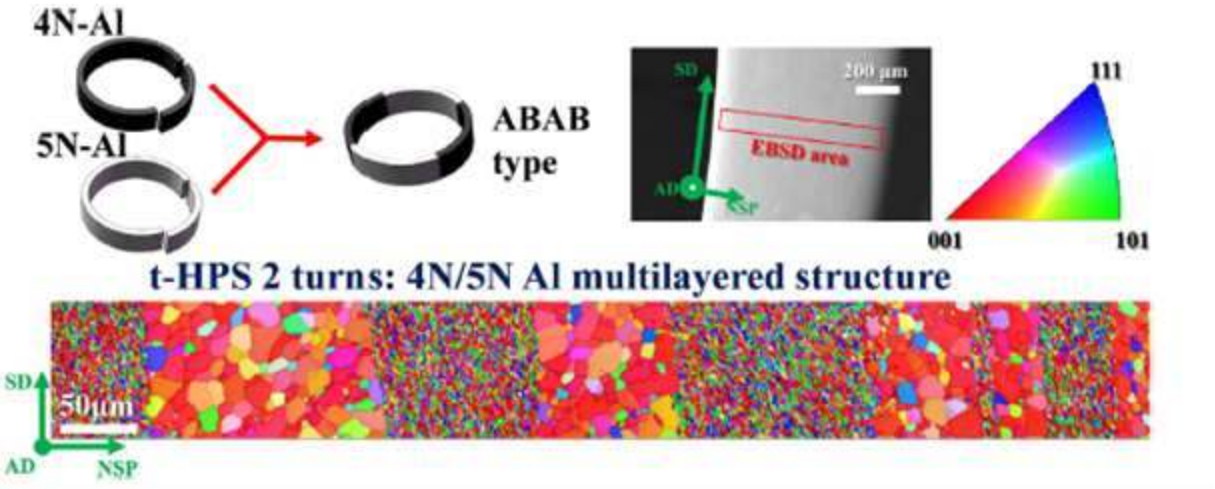

Figure 4. Multilayered structure with alternate distribution of finer and coarser grains fabricated by an ABAB-type 5N-Al/4N-Al bimetallic tube with 2 turns of t-HPS at RT: the 4NAl layers have finer grain size (<1 μm) and the 5N Al layers have relatively coarser grains. Reprinted with permission from reference [78].

E. Using HPT to Process Metal Matrix Nanocomposites

Processing by HPT is generally used to achieve grain refinement in bulk solids. However, the same process has been used also to consolidate metallic powders [83-97], composites [98-102], amorphous compounds [103-107], machining chips [108-110] and ceramic powders [111]. Very recently, new approaches have been developed based on using HPT to bond dissimilar metals and produce solid bulk metallic samples.

The use of dissimilar metals is well established in processing by ARB where sheets of different materials may be conveniently stacked and then processed to form multi-layered microstructures [112-116]. But experiments show that processing by ARB leads to anisotropic plastic behavior, including in strength and ductility, because the properties depend critically upon the precise testing direction cut from the finished product [117]. This suggests it may be

advantageous to make use of the very high pressures inherent in HPT processing in order to achieve a solid-state reaction.

The first attempt to bond dissimilar metals using HPT was in experiments where semi-circular half-disks of Al and Cu were successfully bonded by HPT at RT using a total of up to 100 revolutions [118]. Similar experiments were also conducted using four quarter-disks, two each of pure Cu and an Al-6061 alloy, which were positioned to make a complete disk and then processed by HPT for 1 turn at RT to fabricate an Al-Cu hybrid material [119]. This early work confirmed the feasibility of this approach and accordingly extensive experiments were conducted using a commercial purity aluminum Al-1050 alloy and a commercial ZK60 magnesium alloy with the objective of using these materials to synthesize an Al-Mg multi-layered bulk nanostructured material [120-123]. All processing in these experiments was conducted using HPT at RT under quasi-constrained conditions [124,125] with three separate disks placed in the HPT facility in the stacking order of Al/Mg/Al with the Mg disk held between the two Al disks but without using any glue or metal brushing treatment. All stacks of disks were processed under an applied pressure of 6.0 GPa with various numbers of turns up to a total of 10 revolutions using a constant rotation rate of 1 rpm.

Figure 5 shows three color-coded contour maps that display, using different colors, the values of the measured Vickers microhardness recorded on vertical cross-sectional planes of the disks after processing through 1, 5 and 10 turns, respectively [120]. After 1 turn the hardness is of the order of ~60-70 Hv but after 5 turns the hardness has increased at the edges of the disk and this hardness at the periphery increases even more after 10 turns. Thus, the hardness increases to Hv ≈ 130 at the edge after 5 turns but it further increases to Hv ≈ 270, equivalent to a tensile strength of ~865 MPa, after 10 turns. These hardness values are exceptionally high and they

may be compared with values of *Hv* ≈ 63-65 [126] and *Hv* ≈ 105-110 [127] for the Al-1050 alloy and the ZK60 alloy, respectively, after processing by HPT through 5 turns. Detailed examination by transmission electron microscopy and energy-dispersive X-ray spectroscopy revealed that this high hardness is due to the formation of intermetallic nano-layers of β-Al_3Mg_2 and the development after 10 turns of a nanostructured intermetallic compound of γ-$Al_{12}Mg_{17}$ in the Al matrix in a supersaturated solid solution state. The extraordinary strength achieved in these experiments through HPT processing of disks of dissimilar metals suggests there is a potential for using this approach to fabricate a wide range of metal matrix nanocomposites (MMNCs).

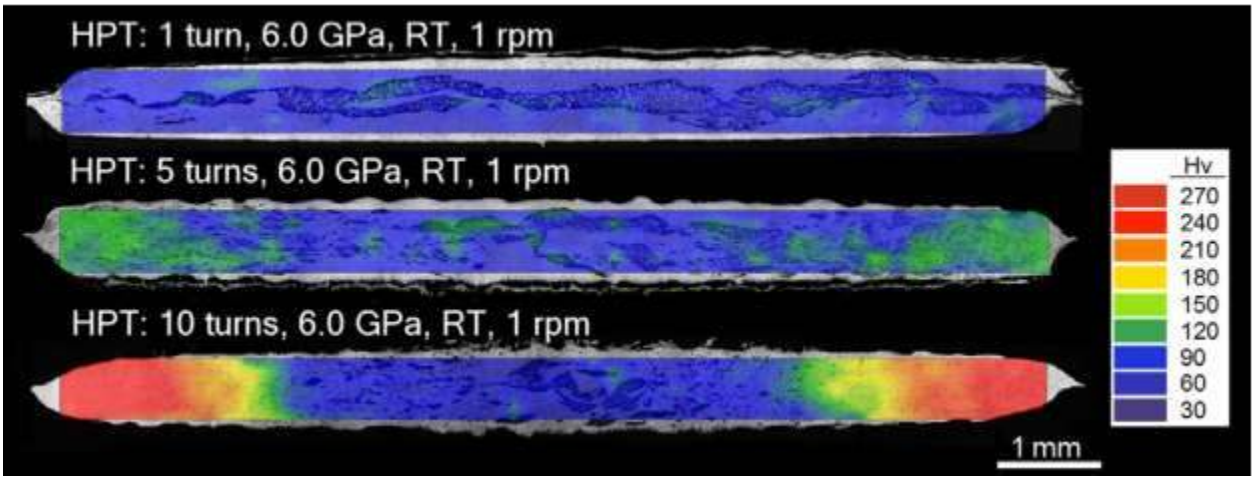

Figure 5. Color-coded contour maps of the Vickers microhardness for the Al/Mg system after HPT for 1 turn (upper), 5 turns (center) and 10 turns (lower): the values associated with the various colors are given in the hardness color key on the right. Reprinted with permission from reference [120].

Using the tensile strength of ~865 MPa at the edges of the disk in Fig. 5, the measured strength at the outer edge after 10 turns gives a remarkable strength/weight ratio of ~350 MPa cm^3 g^{-1} and this specific strength is much higher than in many steels or Ti alloys and it is even

comparable to some strong polymeric engineering composites [128]. Therefore, using the diagram proposed earlier for a very wide range of materials as shown in Fig. 6 [128], it is now appropriate to include the experimentally-synthesized Al-Mg system shown in Fig. 5 where this is denoted in the diagram as HPT-induced aluminum MMNCs without delineating any upper limits to the fracture toughness or the strength-to-weight ratio [122]. It is important to note, from inspection of Fig. 6, that the new MMNC is far superior to conventional Al and Mg alloys (shown by the regions in yellow and red, respectively). Although detailed experiments will be required in the future to precisely define the limits of this approach, it is clear from these early observations that HPT processing of dissimilar metals has a considerable potential for fabricating MMNCs having unusually high strength.

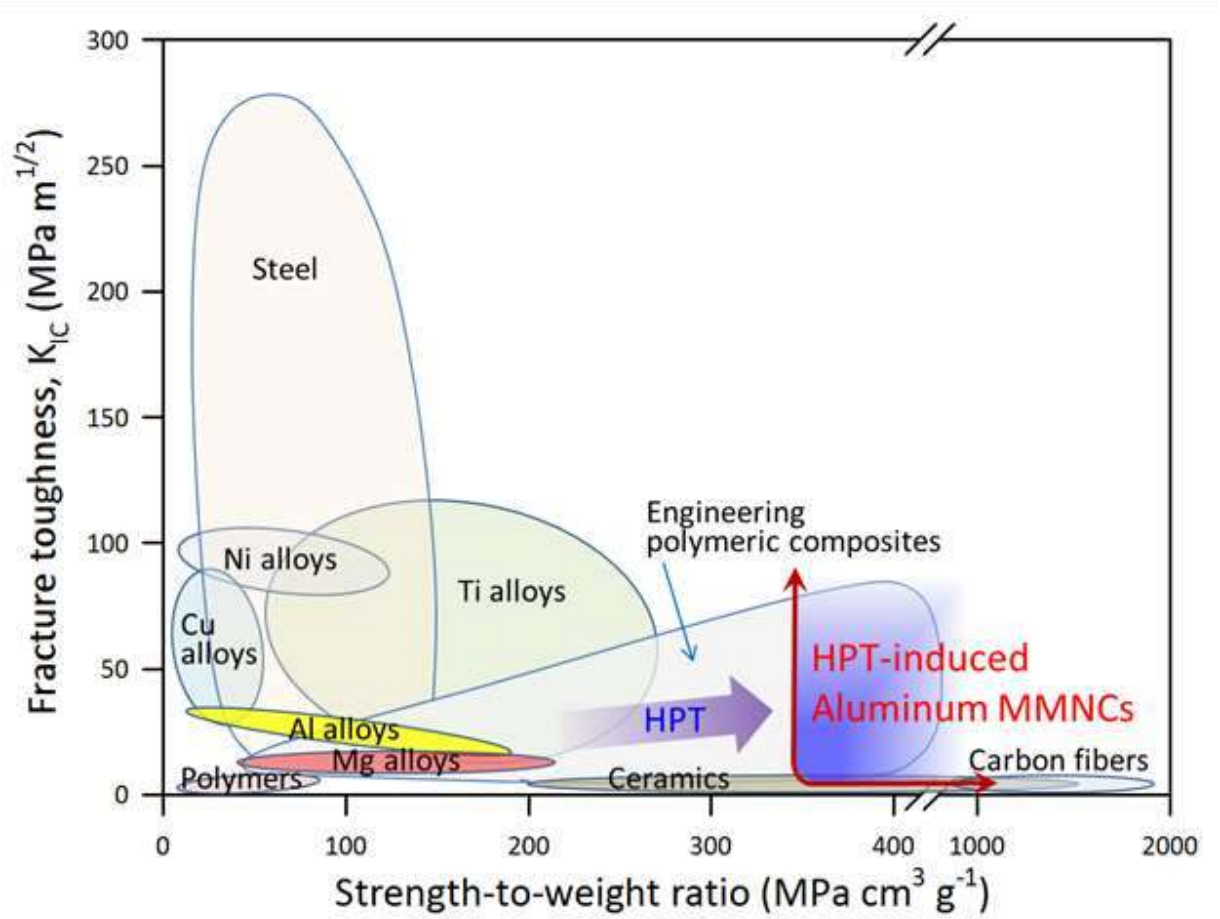

Figure 6. The range of fracture toughness and strength-to-weight ratio for many metals and materials [128] where the synthesized Al-Mg system shown in Fig. 5 after HPT is incorporated into the diagram as HPT-induced aluminum MMNCs without delineating any upper limits for these values. Reprinted with permission from reference [122].

III. BULK NANOSTRUCTURED MATERIALS FROM POWDER PRECURSORS –THE NEED FOR GRAIN SIZE STABILIZATION.

Because grain boundaries are non-equilibrium defects and increase the free energy of a material, the large area of grain boundaries in nanostructured materials provides a large driving force for grain growth. The nanocrystalline grain size is inherently unstable. Significant grain growth, that is, doubling of the initial nanocrystalline grain size in 24 hours, has been observed at room temperature in a number of pure, relatively low melting temperature elements such as Sn,

Pb, Al, and Mg [129]. Günther et al. [130] studied grain growth in pure Cu, Ag, and Pd and found grain growth occurring at much lower temperatures than those observed for recrystallization of the elements after heavy cold deformation. In fact, grain growth in Cu and Pd was observed even at room temperature. This is particularly dramatic for Pd which has a high melting temperature of 1825K (1552^{o}C) such that room temperature is only 0.16 of the melting temperature – a very low homologous temperature. Subsequently, Ames et al. [131] observed the grain growth of 10 nm grain size Pd to 10 micron grain size after one month at room temperature. In this case, as in the others of grain growth at room temperature, the initial growth is abnormal. However, at longer times the grain growth changes to normal grain growth.

A general expression for grain growth in terms of the velocity of the boundary can be given as: $V = MP$ where M is the grain boundary mobility = $M_o \exp(-Q_m/RT)$, and P = the driving pressure = $C\gamma/r$, where γ is the specific grain boundary energy, and r is the average grain radius.[132,133]. The two approaches for achieving stabilization of nanoscale grain sizes are then to 1, reduce the mobility, M, by various pinning mechanisms, or 2. To reduce the driving force for grain growth by reducing the specific grain boundary energy, γ.

A. Kinetic stabilization theories and examples of experimental evidence

There are a number of possible mechanisms that have been proposed that may limit the mobility of nanocrystalline grain boundaries. These include porosity drag, solute drag, second phase (Zener) drag, chemical ordering, and grain size stabilization. The most general applicability to a variety of systems and the most important of these mechanisms are solute drag and second phase (Zener) drag.

First we discuss the solute drag mechanism. The Cahn [134] Lucke-Stuwe [135] models provide good semi-quantitative account of the effects of solute on grain boundary mobility. According to these models, at low velocities the velocity is inversely proportional to solute concentration. At higher driving forces or lower solute concentrations, there is a transition to a velocity regime where the velocity is independent of solute content. The effect of solute is less at higher temperatures. The solute atmosphere becomes much weaker. Solute drag has been used to explain experimental results of stabilization of a number of nanocrystalline materials, for example Ni-1 at.% Si [136] and Pd – 19 at.% Zr [137].

In the second phase (Zener) drag mechanism, the second phase may be a precipitate or dispersoid (e.g. oxide). This pinning effect is less sensitive to temperature than solute drag, especially if a dispersoid is resistant to coarsening. Particle size and distribution play a key role in the effect. The expression for the pinning pressure exerted on the grain boundary by small particles is, in the original Zener formulation [132]

$P = 3f\gamma/2r$, where f is the volume fraction of particles randomly distributed of spherical radius r, and γ is the specific grain boundary energy. A refinement of this model [138] gives $D = 0.17d/f$ for low volume fractions, where D is the critical grain size, d the particle size, and f the volume fraction. A large number of experiments on stabilization of nanocrystalline grain sizes have been explained using Zener drag, for example Fe – 10 Al with dispersoids [139].

Other mechanisms for decreasing grain boundary mobility include porosity drag, chemical ordering, and grain size effect. Porosity can reduce grain boundary mobility as demonstrated in the grain growth of ceramic TiO_2 prepared by the inert gas condensation method [140]. Reduced grain growth has been observed for ordered nanocrystalline intermetallic compounds, for example Fe_3Si [141]. Grain size stabilization has been predicted by theoretical models and

observed experimentally [142]. It is suggested that the decrease in free volume which occurs on grain growth is offset by the non-equilibrium vacancy concentration increases in the matrix as the excess free volume is released on grain growth.

B. Thermodynamic stabilization theories

The general concept of thermodynamic stabilization involves the segregation of solute atoms to the grain boundaries such that the grain boundary energy may be reduced. The reduction of excess interface Gibbs free energy, G, with increasing solute content can be described by the Gibbs adsorption isotherm: $d\gamma = -\Gamma d\mu$ where μ is the chemical potential of the solute atom dissolved in a matrix of solvent atoms, and Γ is the excess amount of solute atoms segregated to the boundary. Plots of $\gamma = dG/dA$ vs. global solute content show a reduction of γ with increasing solute content [143]. Large solute atoms intensify this and could reduce the excess grain boundary free energy with possible grain boundary stabilization at $\gamma = 0$. This γ is not to be confused with grain boundary cohesive energy. Weissmuller [144] was the first to apply these ideas to stabilization of nanocrystalline grain size. His model was based on a dilute solution limit. The equation has the following form: $\gamma = \gamma_o - \Gamma_{sat}[\Delta H_{seg} + RTln\ (x_c)]$ where γ_o is the grain boundary energy of the pure metal, Γ_{sat} is the solute excess for fully saturated grain boundary interface, ΔH_{seg} is the segregation enthalpy, and $RTln(x_c)$ represents the ideal mixing entropy for bulk solute concentration x_c. This equation implies that the grain size at stabilization decreases as the solute content increases at a fixed temperature. The analysis of Weissmuller was extended by Kirchheim [145] to include the temperature dependence of grain size for a metastable equilibrium state. The regular solution model of Trelewicz and Schuh [146] eliminates many of the approximations in the previous models, for example, fully saturated grain boundaries or dilute solution approximations. This model has grain boundary regions and bulk

426 regions with variable volume fractions and solute concentrations separated by transitional bonds.
427 ΔG_{mix} is obtained from the difference in the nearest neighbor bond energy and mixing entropy of
428 this system relative to equivalent volumes of unmixed pure A and pure B with no grain
429 boundary. The equilibrium state is obtained by simultaneous minimization of ΔG_{mix} with respect
430 to variations of the solute concentration and the grain boundary volume fraction, subject to
431 conservation of solute. Elastic size misfit enthalpy was not included in this model. A
432 modification of the above model was presented by Saber et al. [147]. A regular solution model
433 for thermodynamic stabilization was based on the Wynblatt-Ku approximation [148] to
434 incorporate both chemical and elastic enthalpy. The equilibrium condition is defined by
435 minimization of the total Gibbs mixing free energy with respect to simultaneous variations in the
436 solute contents and volume fractions with the constraint of overall mass balance. The Lagrange
437 multiplier technique was used to obtain an explicit solution to the constrained equations in a
438 form easily solved using standard numerical software packages. Results for Fe-Zr alloys are
439 given in Figure 7 [147].
440

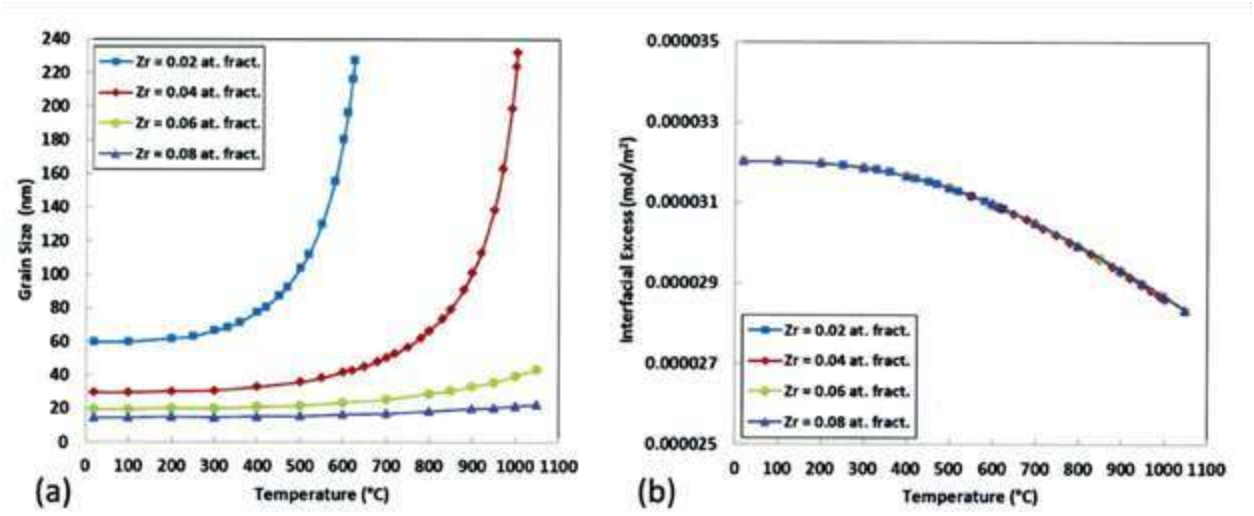

Figure 7. Model predictions of (a) grain size, and (b) interfacial solute excess for Fe-Zr alloys. Reprinted with permission from reference [147].

The previous models did not consider the competition with precipitation of second phases or phase separation. Chookajorn et al. [149] addressed this problem using an analytical approach based on the Trelewicz and Schuh [146] model. They simplified the problem by considering only alloys with positive enthalpies of mixing. Stability maps of enthalpy of segregation vs. enthalpy of mixing were constructed for several elements. One for tungsten is shown in Figure 8.

Subsequently, Schuh and co-workers have extended the range of alloys and details of the grain boundary structure by using Monte Carlo simulations to construct stability maps with six different regions of nanocrystalline stability including duplex nanostructures [150].

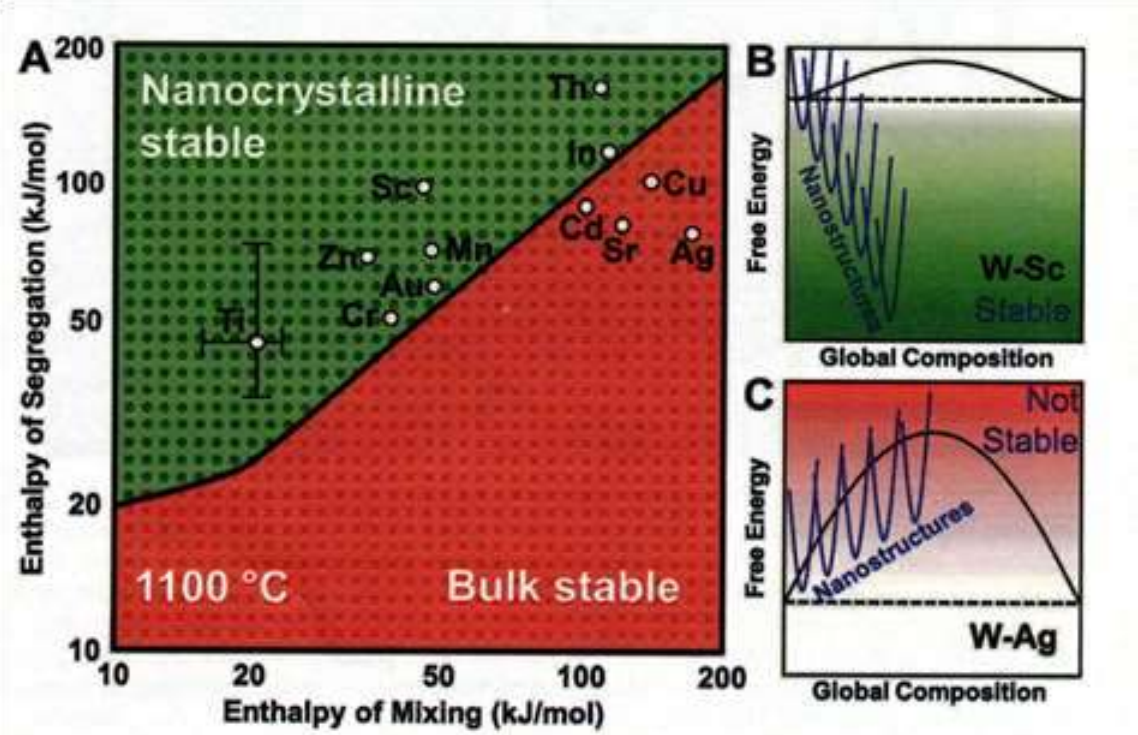

Figure 8. The nanostructure stability map for tungsten-based alloys at 1100oC, calculated on the basis of variation of the enthalpy parameters. For each combination of parameters, the free energy of nanocrystalline structures is compared to that of the bulk regular solution. An example for the nanocrystalline stable region in given in (B) for W-Sc. A bulk stable case is given in (C) for W-Ag. Reprinted with permission from reference [149].

C. Complexions as possible sources of nanocrystalline grain size stabilization

Interface "complexions" are grain boundary "phases" in thermodynamic equilibrium that have stable, finite thicknesses. They were first, and mostly, observed and studied in ceramic materials. Dillon et al. [151] have created a categorization scheme for complexions based on studies of Al_2O_3 doped with calcia, silica, magnesio, or neodymia. The six categories of complexions were identified using high resolution TEM images of the grain boundaries. Rupert [152] has recently reviewed the role of complexions in metallic nanocrystalline materials with regard to thermal stability and deformation. Khalajhedayati and Rupert [153] had reported remarkable thermal stability in nanocrystalline Cu – 3at.% Zr with a nanoscale (54 nm) grain

size remaining after heating for a week at 1223K (950°C) (98% of the solidus temperature!). They attributed this stability to segregation at the grain boundary forming amorphous intergranular films (complexions) and to Zener pinning by ZrC nano-particles.

D. Experimental evidence for thermal stability of nanocrystalline alloys

A few examples were given in the section on kinetic stabilization theories of experiments that appear to support this mechanism. In this section, two examples of systems will be given where there is possible contributions to thermal stabilization from both the thermodynamic and kinetic mechanisms. Finally, a comparison will be made using the available data from the literature of thermodynamic, kinetic, combinations of the two, and complexions for stabilization of nanocrystalline alloys as a function of homologous temperature.

Example 1. Thermal stability of nanocrystalline Fe-Cr alloys with Zr additions. The influence of 1 to 4 at.% Zr additions to Fe – 10 and 18 at.% Cr alloys on the thermal stability of the nanocrystalline microstructure was studied [154]. Grain sizes were determined by XRD, channeling contrast FIB imaging, and TEM for isochronal annealing treatments up to 1273K (1000°C). Grain size stabilization in the nanoscale range was maintained up to 1173K (900°C) by adding 2 at.% Zr. This is illustrated in Figure 9 where a histogram of the bright field TEM grain size data is given for the Fe – 10 at.% Cr – 2 at.% Zr sample annealed at 1173K. The average grain size for this condition was determined to be 82 nm. Analysis based on the Hall-Petch strengthening and Orowan strengthening was used to extract the volume fraction of intermetallic particles having a mean size of 20 nm. Comparing the TEM grain size with the calculated grain size from the Orowan hardening and Zener pinning models of 168 nm suggests that thermodynamic stabilization may be contributing to the stabilization observed along with Zener pinning.

There was no significant difference in the results for the 10 and 18 at.% Cr alloys, which indicates that the bcc to fcc phase transformation does not influence the grain size stabilization in these alloys.

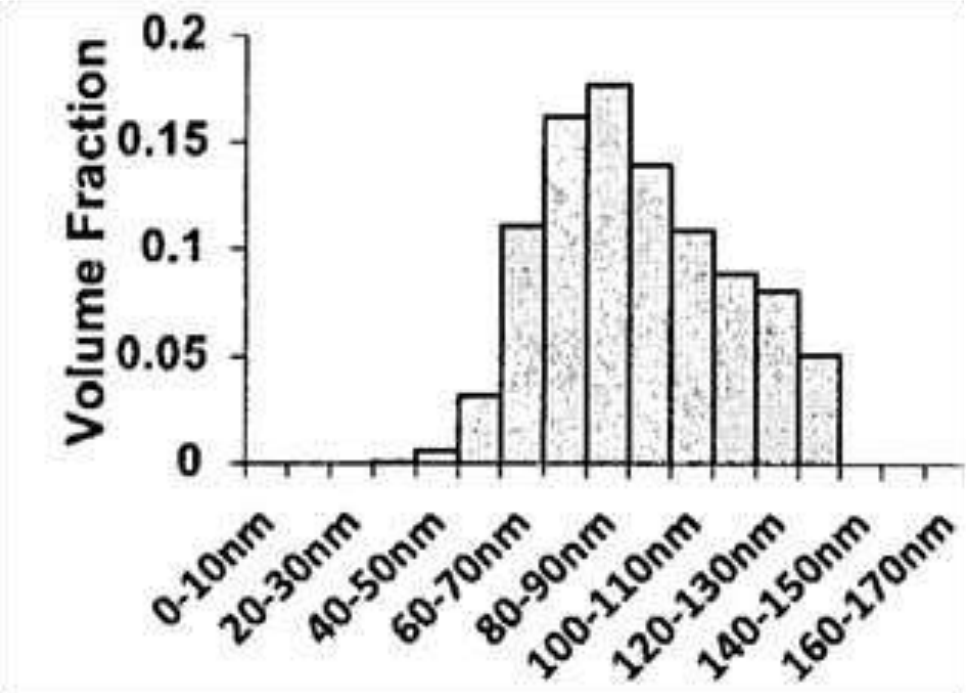

Figure 9. Bright field grain size histogram for Fe – 10 at.% Cr – 2 at.% Zr sample annealed at 1173K (900˚C). Reprinted with permission from reference [154].

Example 2: High temperature grain size stabilization of nanocrystalline Fe-Cr alloys with Hf additions. Similar to example 1, the influence of 1 to 4 at.% Hf additions on the thermal stability of nanocrystalline Fe – 14 Cr was studied [155]. Hf was selected as a solute addition because the enthalpy of formation of HfO_2 is more negative than that of ZrO_2 indicating that the second phase formation leading to Zener pinning effect might be enhanced compared to the Zr solute additions in Example 1. In addition, the prediction of thermodynamic stabilization for ternary alloys [156] suggests that Hf should be an effective solute for thermodynamic stabilization in Fe -14Cr. Again, XRD, high resolution TEM, channeling contrast FIB imaging, and microhardness

508 were obtained for isochronal annealing temperatures up to 1373K(1100^{o}C). It was found that the
509 Fe – 14Cr – 4 at.% Hf alloy exhibited effective grain size stabilization in the nano-scale range up
510 to 1273K (1000^{o}C). The hardness of nearly 5.2 GPa is maintained after annealing at 1273K.
511 The Hall-Petch plot for this alloy along with the base Fe – 14Cr alloy is presented in Figure 10.

512 Employing the Hall-Petch grain size strengthening and Orowan particle strengthening
513 equations for Fe – 14Cr – 4 at.% Hf annealed at 900^{o}C, the deviation of grain size predictions
514 from the actual grain size suggests , as in Example 1, the possibility of a thermodynamic
515 stabilization mechanism contribution due to solute segregation to grain boundaries. The use of a
516 thermodynamic model [156] (prediction given in Figure 11) shows that thermodynamic
517 stabilization can be a viable additional mechanism in conjunction with Zener pinning for
518 stabilizing the nano-grains in Fe - 4Cr – 4 at.%Hf at 1173K (900^{o}C).
519

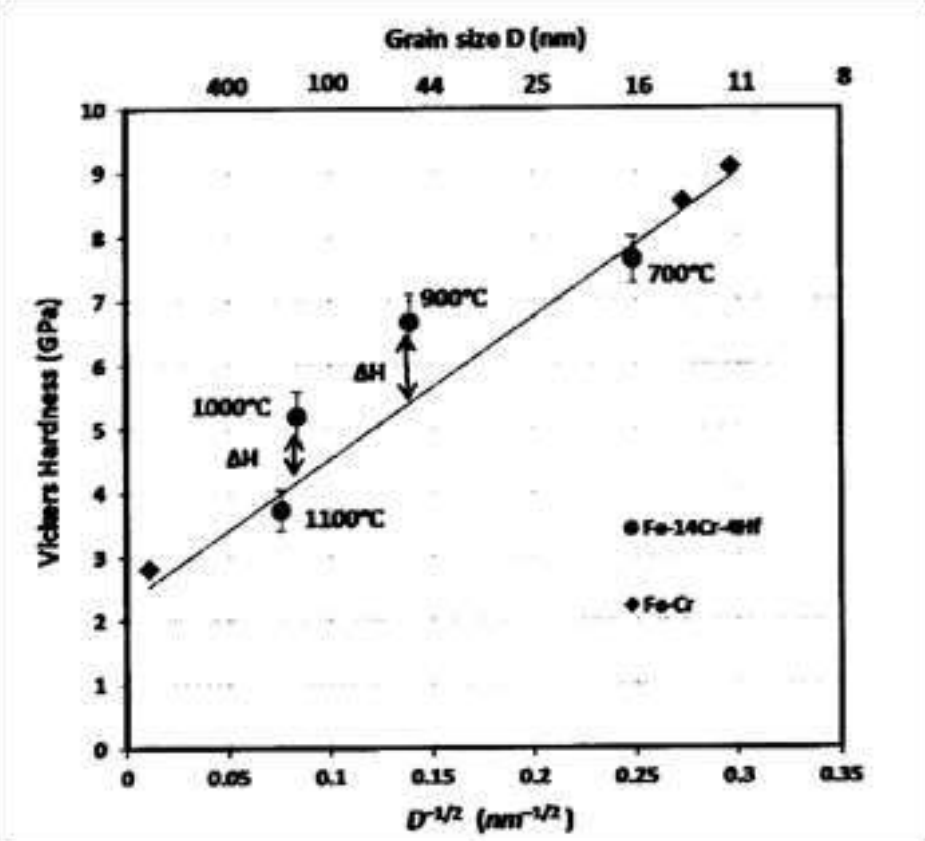

Figure 10. Hall-Petch plot of Fe – 14Cr – 4Hf alloy along with the base Fe – 14Cr alloy. Reprinted with permission from reference [155].

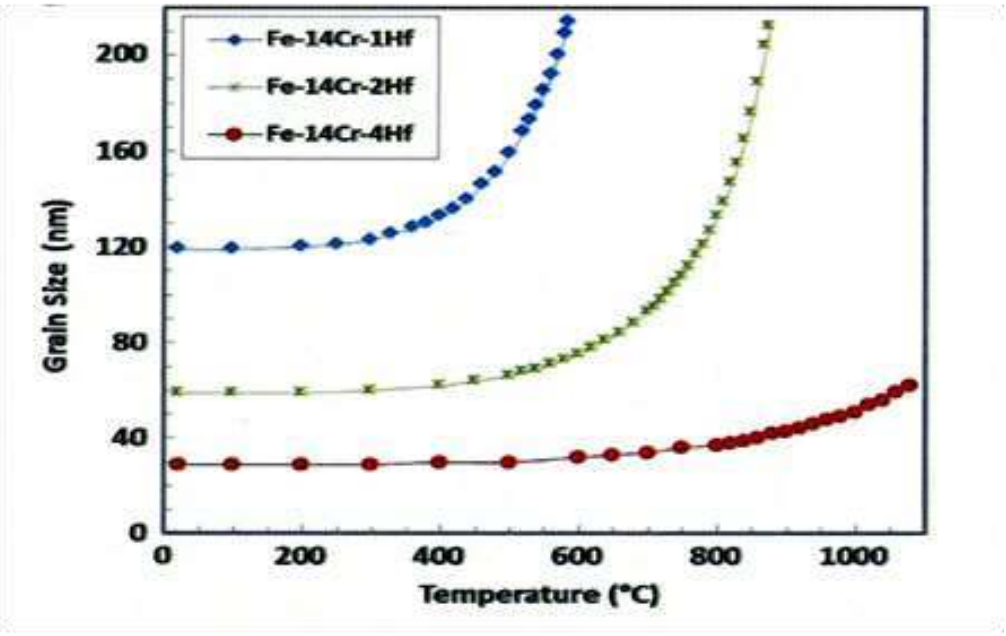

Figure 11. Model prediction for Fe – 14Cr – x Hf alloys for grain size. Reprinted with permission from reference [155].

To summarize this section on the thermal stabilization of nanocrystalline materials we examine data from the literature and looking at the maximum homologous temperature for which the alloy remains nanocrystalline (grain size < 100 nm) and the specifics of the experimental results decide whether the stabilization was due to the thermodynamic mechanism, a kinetic mechanism, a combination of the two, or due to kinetic and complexion stabilization.

From the experimental data shown in Figure 12, it would suggest that the most effective mechanisms for thermal stabilization of nanocrystalline grain size are kinetic (Zener pinning by nanoscale particles) or a combination of this and thermodynamic stabilization by solute segregation to grain boundaries. The one data point for Cu – 3 at.% Zr where Zener pinning is combined with the complexion (an amorphous grain boundary layer) that gives thermal stabilization almost to the melting temperature, points to a possible fertile research field to improve the properties of nanocrystalline alloys.

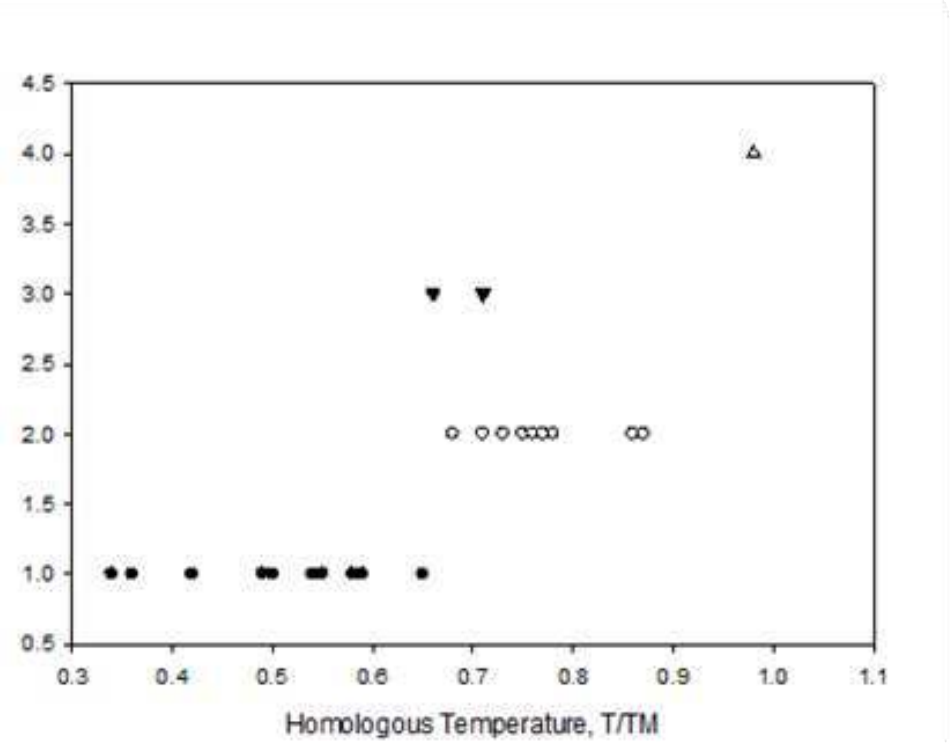

Figure 12. Literature data for thermal stabilization mechanisms vs. maximum homologous temperature for stabilization. The symbols are: thermodynamic stabilization: ●, kinetic stabilization: ○, kinetic and thermodynamic stabilization: ▼, kinetic and complexion stabilization: Δ

IV. CRYOMILLING AND APPLICATIONS

Cryomilling, i.e., mechanical milling of alloys at cryogenic temperatures is representative of a class of powder synthesis techniques that attain the nanostructured state via severe plastic deformation. The cryogenic milling process has attracted considerable interest, primarily as a result of its ability to generate nanocrystalline (NC) and non-equilibrium structures in relatively short time and large quantities. Cryomilled NC powder that can be used to manufacture bulk nanostructured and ultrafine-grained (UFG) alloys with attractive combinations of physical and mechanical properties. Inspection of the scientific literature shows that this technique has been widely used to synthesize NC metals, alloys, and composites, such as Al [157-159] , Ni [160]

557 Fe [161], Ti [162], Zn [163], Mg [164,165], Pd-10Rh [166], high entropy alloys (HEAs)
558 [167,168], and Al-B_4C/SiC composites [169,170]. In certain fcc materials, cryomilling can
559 promote deformation twinning, which is beneficial, given that deformation twins provide for
560 strength enhancement without a loss in ductility. Cryomilling in a liquid nitrogen environment
561 facilitates the formation of nitrogen-containing dispersoids that substantially increase the thermal
562 stability of nanostructures. Thermal stability is critical to retaining fine grain sizes during
563 consolidation of the cryomilled powder when subjected to temperature and pressure. The use of
564 light-weight, higher-strength alloys, such as NC Al alloys, for the construction of vehicles will
565 substantially reduce their weight and lead to improved fuel consumption, range, reliability, and
566 speed. In this section, published data related to cryomilled alloys are reviewed with particular
567 emphasis on cryomilling mechanisms, microstructure, deformation twining, thermal stability of
568 cryomilled powders, and some examples of practical Al alloys fabricated by cryomilling and
569 consolidation.

570 *A. Cryomilling*

571 During cryomilling, the as received powder forms a slurry with a milling attritor, comprising
572 of a rotating impeller within a vessel, and accommodating a flow of incoming cryogenic liquid,
573 normally liquid N_2 or liquid Ar. In the laboratories at UC Irvine (Irvine, CA), the system with
574 the largest capability can mill up to 5 kg of Al alloy powder at a time, but there is potential to
575 substantially increase the scale of this operation for commercial exploitation.

576 During cryomilling, similar to conventional mechanical milling, the particles of the powder
577 are repeatedly deformed by compressive and shear stresses arising from being trapped between
578 the balls during collisions and localized rolling. Powder evolution during the milling process
579 generally involves five stages [157,158]: 1) initially, particle flattening as a result of shear band

nucleation under localized deformation conditions [171], which then spread throughout the entire sample, forming flakes; 2) when two or more particles are trapped between the balls, they are crushed and cold-welded together to form particles of a larger size with a lamellar structure; 3) equiaxed particle formation due to fracture deformed particles; 4) random welding of powder particles; and 5) steady-state deformation, during which a balance between fracture and cold welding is established as particle size and microstructural refinement progresses. Given that severe plastic deformation during milling is a cyclic process, the milling time dominates the overall deformation strain.

Cryomilling leads to the formation of a high density of dislocations in the cryomilled powder because milling induces heavy cyclic deformation, and the cryogenic temperature suppresses the annihilation of dislocations. As an example, a high density of dislocations of 1.7×10^{17} m^{-2} was observed in a cryomilled Al–Mg alloy [172,173]. The dense dislocation networks rearrange to form nanoscale subgrains with low-angle grain boundaries (GBs) during further milling, and then re-orient and transform into grains with high-angle GBs. With an increase in milling time, the mean grain size initially decreases rapidly from the micrometer scale, then slowly decrease down to a saturated value, a few tens of nanometers, determined by the material properties [174, 175]. When a minimum grain size is reached, additional straining does not further reduce the grain size because of the intrinsic instability of nano-sized grains. Thus, strain-induced grain refinement ceases as a dynamic balance is reached between structure refinement and coarsening of the refined grains.

The value of the minimum grain size that is attained during milling is related to the intrinsic properties of the materials [174] as well as the milling conditions. It has been proposed that the minimum grain size obtainable by milling scales inversely with melting temperature and bulk

603 modulus of a material. To that effect a dislocation model was developed to quantitatively
604 describe the minimum grain size obtainable during milling [175]. According to this model, the
605 minimum grain size is governed by the balance between the hardening rate introduced by
606 dislocation generation, and the recovery rate arising from dislocation annihilation and
607 recombination. The minimum grain size, d_{min}, is given by [175]:

608 $$\frac{d_{\min}}{b} = A_3 \exp\left(\frac{-\beta Q}{4RT}\right)\left(\frac{D_{PO} G b^2}{v_0 k_B T}\right)^{0.25}\left(\frac{\gamma}{Gb}\right)^{0.5}\left(\frac{G}{\sigma}\right)^{1.25} \quad (2)$$

609 where b is the magnitude of the Burgers vector, A_3 a dimensionless constant, β constant, Q the
610 self-diffusion activation energy, R the gas constant, T the absolute temperature, D_{PO} the diffusion
611 coefficient, G the shear modulus, v_0 the initial dislocation velocity, k_B Boltzmann's constant, γ the
612 stacking fault energy (SFE) and σ is the applied stress. The model predicts that the minimum
613 grain size scales inversely with hardness, proportionally with the SFE and exponentially with the
614 activation energy for recovery.

615 Grain refinement may also occur via recrystallization when a new grain structure forms by
616 nucleation and growth in cold deformed alloys with sufficient stored energy. It is generally
617 argued that recrystallization is not able to occur during cryomilling because recrystallization is
618 thermally activated and depends on a critical temperature and deformation conditions.
619 Interestingly, however, it has been reported that recrystallization does indeed occur in cryomilled
620 Zn [163] and Mg [176]. High density of lattice defects, including stacking faults [177],
621 dislocation, deformation twins [178], and increased GBs generated due to heavy deformation in
622 cryomilled NC hexagonal close packed (HCP) Mg alloys have been reported. In fact, the high
623 density of accumulated lattice defects, particularly dislocations, results in a high stored energy, E
624 $= Gb^2\rho$, which may trigger dynamic recrystallization (DRX) even at cryogenic temperatures. In

addition, a high density of dislocations causes the critical temperature for recrystallization T_c to decrease. Recrystallization of cryomilled Mg powder in liquid Ar may also be thermally activated at room temperature due to the presence of relative elevated temperatures (88 K to 298 K) when the cryomilled Mg powder is collected at room temperature. The conditions for nucleation of DRX are described by [179]:

$$\frac{\rho^3}{\dot{\varepsilon}} > \frac{2\,\gamma_b}{KMLG^2b^5} \quad (3)$$

where ρ is the dislocation density, $\dot{\varepsilon}$ is the strain rate. γ_b is the specific boundary energy, M is the grain boundary mobility, L is the mean slip distance of the dislocations, G is shear modulus, b is Burger vector, K is a constant. There is a critical value of $\rho/\dot{\varepsilon}$ to be achieved for the nucleation of DRX. When materials with a low SFE, such as Zn, Mg and their alloys with low SFE are deformed at cryogenic temperature, dislocation recovery is slow and the dislocation density could be increased to the critical value necessary for facilitating DRX.

The cryomilling technique possesses several characteristics and advantages that distinguish it from the conventional mechanical milling that is typically performed at ambient temperatures, including: 1) powder agglomeration and welding to the milling media are suppressed, resulting in a more efficient milling outcome; 2) oxidation reactions during milling are reduced under the protection of a liquid nitrogen or argon environment; 3) the milling time required to attain a nanostructure is significantly reduced relative to that required of conventional milling. Figure 13 shows a comparison of the average grain size evolution with milling time for Zn powder milled at room temperature and at liquid N_2 temperature [179]. It has been consistently reported that the average grain size of cryomilled Zn is consistently smaller than that of room temperature milled Zn with the same amount of milling time. Cryomilling takes the advantage of the

extremely low temperature of the liquid N_2 or Ar medium, which suppresses the recovery and leads to more rapid grain refinement and finer grain structures. In addition, the lower temperature also decreases the ductility of the powder, reducing the amount of welding between the particles. Thus, the amount of process control agent (PCA) required to prevent excessive agglomeration of the particles is reduced, decreasing the amount of interstitial contamination introduced during the milling process.

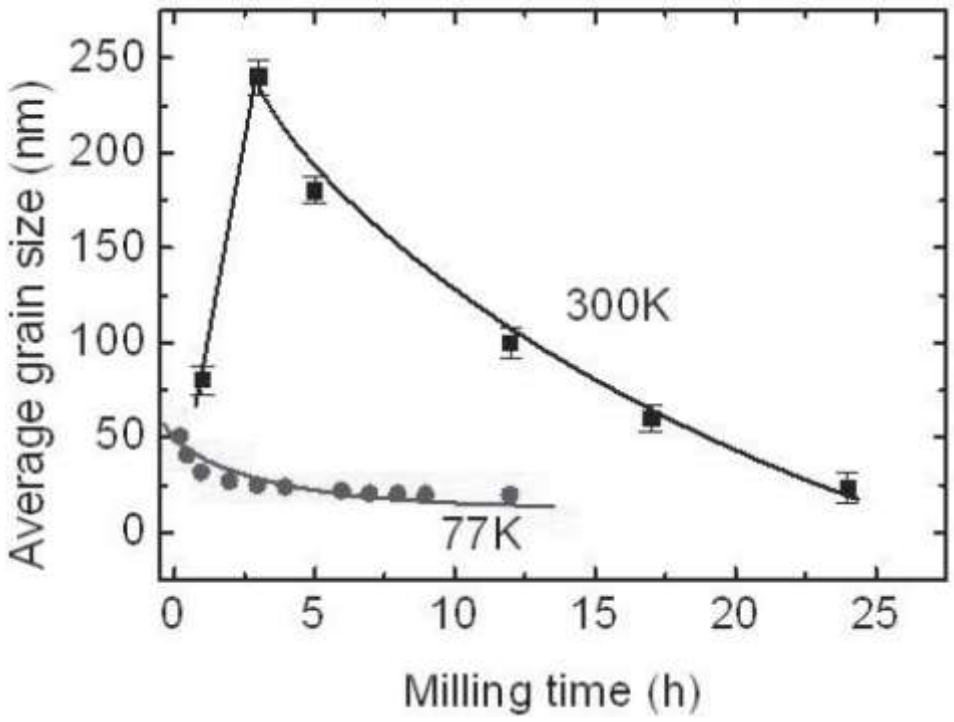

Figure 13 Comparison of the average grain size evolution with milling time for Zn powder milled at room temperature and at liquid nitrogen temperature. Reprinted with permission from reference [179].

Even in the presence of hard particles, such as in the case of cryomilling of a matrix/reinforcement (typically a ceramic) mixture, the ductile matrix is deformed, flattened and cold welded [174]. During cryomilling the reinforcement particles are entrapped in the matrix

material, which can eliminate the voids between the matrix and the ceramic reinforcement and potentially promote solid state bonding between them. Another advantage of using cryomilling to synthesize metal matrix composite powders is that it facilitates the formation of a homogeneous distribution of the reinforcement particles in the matrix. Conventional blending methods often lead to clustering of the reinforcement, resulting in poor mechanical behavior. Published studies suggest that a homogeneous distributions of reinforcements in a matrix can readily be achieved by using cryomilling 169,170].

In addition, the presence of hard particles in a powder mixture can facilitate deformation and fracture of the matrix and thereby facilitate grain refinement. As a consequence, a shorter milling time may be required to attain steady state conditions during milling. In related studies it was reported that the introduction of a small volume fraction of AlN particles (2 μm) into Ni facilitated grain refinement during cryomilling [180]. This enhancement was rationalized on the basis of the interactions of dislocations with hard particles, and the thermally induced dislocation generation due to the difference in thermal expansion coefficient between matrix and reinforcement [180,181].

B. Deformation Twining by Cryomilling

It is well known that NC alloys are significantly stronger than their coarse-grained counterparts [157,182], but their ambient temperature uniform tensile ductility is usually disappointingly low due to the fact that GBs experience much larger plastic strain than that sustained by grain interiors. Attempts to retain or increase the ductility during grain refinement have frequently resulted in reduced strength [182,183]. However, it was reported that dislocation accumulation at twin boundaries in NC metals provides strength enhancement without a loss in ductility [184,185]. Twin boundaries with extremely low excess energy can effectively hinder

685 dislocation motion, acting as stable interfaces leading to the increase of both the strength and
686 ductility in NC materials [186,187]. Moreover, it has been well documented that a smaller grain
687 size impedes deformation twinning and there are many experimental studies providing support to
688 this finding [188-191]. On one hand, the stress required for activating twinning increases much
689 faster with decreasing grain size relative to that required for dislocation slip which competes with
690 twinning; accordingly, a smaller grain size renders deformation twinning more difficult. On the
691 other hand, a lower temperature and higher strain rate usually promote deformation twinning
692 [191]. The increase in twinning tendency at low temperatures and higher strain rates can be
693 largely attributed to the increase in flow stress of materials, which increases with decreasing
694 temperature and increasing strain rate. When flow stress increases, the motion of dislocations
695 becomes more difficult, while deformation twining readily occurs. There is an equivalent effect
696 of low temperature and high strain rate, as the dislocation generation rate is faster than the
697 annihilation of dislocation during deformation at low temperature and high strain rates [191]. As
698 cryomilling is characterized by relatively high strain rates (up to 6.35×10^3 s^{-1} [192]) and
699 cryogenic temperatures, deformation twinning is facilitated in cryomilled metals and alloys.

700 In the face centered cubic (FCC) case, the twinning plane is the close-packed (111), and twin
701 nucleation and growth are controlled by well-defined partial dislocations that co-operatively
702 move and propagate on successive (111) planes [194]. A material with high SFE, such as Al
703 (160- 200 J/m^2), will be less susceptible to twinning than materials with low SFE, like Cu alloys
704 (70-78 J/m^2). SFE is equivalent to twin energy, and the propensity for deformation twinning
705 increases with decreasing SFE [195]. Twins are abundant in many low SFE metals, but are rarely
706 seen in high SFE metals like Al [196-198], because when the SFE is low, the mobility of
707 dislocations in a material decreases, while deformation twining become more feasible. Notably,

the first report of twinning in NC fcc Al was observed in cryomilled Al [193], as shown in Figure 14, which shows an HRTEM image of twin with dimension of approximately 10 nm in cryomilled Al-7.5Mg powder. The black arrow shows that atoms on (110) have a strain along <112> direction, and twinning occurred on the (111) plane.

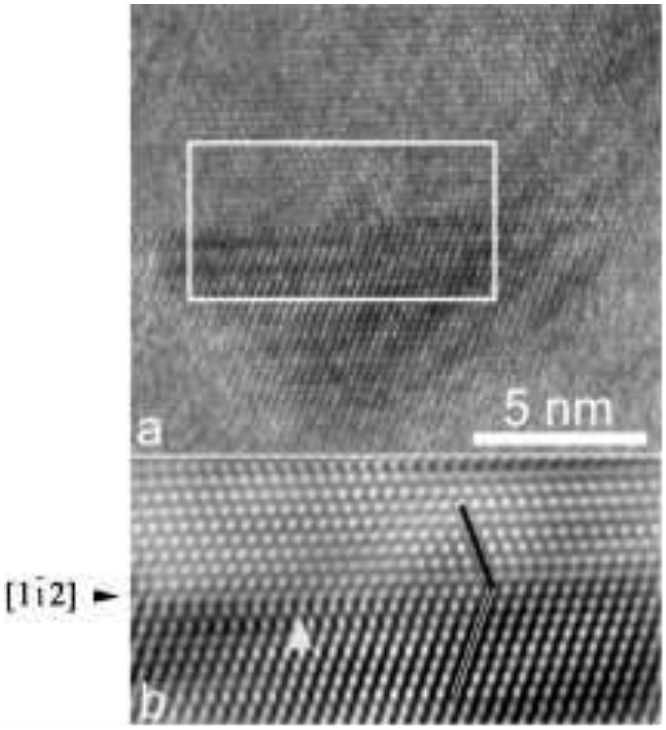

Figure 14 HREM image of Al-7.5Mg alloy cryomilled for 8 h, (a) Image of a whole nanoscale twin. (b) Local magnification of a twin. Reprinted with permission from reference [193].

In most HCP metals and alloys, deformation twins are readily nucleated. This is true, for example, in the case of coarse grained Mg and Mg alloys, due to the low SFE of Mg (30 mJ/m^2 [199]) in combination with a limited number of independent slip systems. The SFE in Mg-(3-9wt.%) Al alloys is 5.8-27.8 mJ/m^2, and decreases with increasing Al content [200]. For HCP Mg, the activation of primary slip system is limited and hindered on account of large CRSS

values at cryogenic temperature. Twinning, however, remains a deformation mechanism that could be activated with secondary slip of partial dislocations under these conditions. The low temperature renders recovery more difficult by limiting the mobility of dislocations [201]. Lattice friction stress also strongly depends on temperature, and increases with decreasing temperature [202], which makes dislocation glide through the lattice and GB sliding more difficult. As deformation intensity increases at cryogenic temperatures with high strain rate, the number of dislocations increases, and a higher dislocation density accumulates on the GB regions, which lead to a highly localized stress concentration at GBs, and act as the driving force for twinning nucleation. In essence, the combination of low temperature and high local stresses that is characteristic of cryomilling promote the activation of twinning mechanisms.

During cryomilling, the flow stress of Mg increases with decreasing temperature and increasing strain rate [203], and accordingly so does the critical stress required to nucleate and propagate a twin. The most commonly observed twinning plane is the (10-12) in the <10-1-1> direction for Mg [204]. This phenomenon has now been documented in a number of NC Mg alloys, such as Mg-10at.%Ti [205], Mg-30wt.%Al [206], as well as cryomilled AZ80 (Mg-8wt.%Al-0.5wt.%Zn)[164]. Moreover the formation of nano-sized twins in cryomilled pure Mg powders was documented using HRTEM [165]. The formation of nano twins in NC pure Mg was attributed to the combination of: a high strain rate, cryogenic temperature, and high local shear stresses present around the GBs during deformation by cryomilling. Such low temperature deformation processing has also been reported to facilitate deformation twinning in other cryomilled NC alloys and ceramics, such as Al-7%Mg [193, 207-209], Cu [210], and B_4C [211]. The formation of twins by cryomilling provides a promising approach to improve the mechanical properties of NC metals and alloys.

C. Thermal Stability of Cryomilled Alloys

NC metals and alloys are thermally unstable when compared to the behavior of their coarse-grained counterparts. From a thermodynamic viewpoint, nano-grains grow at lower temperatures than those required by their coarse grained counterparts [212,213]. There is a large amount of enthalpy that is stored in the high-density GBs, which provides a substantial driving force for grain coarsening [186]. The reduced thermal stability of nanostructured materials not only limits their technological and practical applications, but also renders their processing a challege.

A review of the literature reveals that there are kinetic and/or thermodynamic strategies that have been proposed in an effort to stabilize metallic nanostructures [213]. One approach involves the pinning of GBs by promoting the drag of second-phase, solutes, and chemical ordering [214] in order to decrease their mobility for kinetic stabilization. From a thermodynamic perspective, the driving force of grain coarsening is proportional to the grain-boundary energy. The specific grain-boundary energy can be reduced by solute segregation in the GBs, resulting in a high entropy GBs[214,215]. A theoretical framework that incorporates the influence of second-phase particles and solute segregation at GBs on stress-induced GB migration and grain rotation was formulated [216]. The modelling results suggest that both second-phase particles and solute atoms segregated at GBs reduce the rate of GB migration and grain rotation.

Cryomilling in a liquid N_2 environment generates nitrogen containing nano-sized dispersoids are formed [217-219] which can increase the strength of the alloys by pinning dislocations [161]. The significance of the nitrogen-containing dispersoids is that they substantially increase the thermal stability of the microstructure for Al-containing alloys [219-221]. This is important in retaining fine grain sizes during consolidation when the cryomilled powder subjected to

767 temperature and pressure, the combined effects of which would otherwise lead to rapid grain
768 growth.

769 A low ductility and limited thermal stability represent intrinsic limitations of NC structural
770 materials. Stabilizing nanostructures by interface complexions to decrease the grain-boundary
771 mobility does not improve their ductility. It is necessary to provide work-hardening and strain
772 delocalization during deformation in the nanostructures to enhance their ductility [186]. In
773 related work it has been reported that twin boundaries with extremely low excess energy
774 effectively hinder dislocation and GBs motion and can thus act as stable interfaces. Twin
775 boundaries with nanoscale spacing are effective to improve strength, ductility and thermal
776 stability. This might be another reason for the observed high thermal stability of cryomilled
777 nanostructured materials because cryomilling can promote deformation twining [9, 37].

778 There are numerous published studies documenting the thermal stability of cryomilled alloys.
779 For example, in the case of cryomilled 5083 Al alloy processed via HIP and extrusion results
780 from creep tests at two temperatures: 573 and 623 K [222] show surprising thermal stability. An
781 average grain size of 200 nm was observed in the microstructure of the cryomilled 5083 Al.
782 After a long time exposure for nearly 1000 h at temperatures of 573 and 623 K (0.61–0.66T_m,
783 where T_m is the melting temperature of the materials), there is only a slight grain growth. An
784 average grain size of approximately 220 nm and an average grain size of approximately 280 nm
785 were observed after holding for 996 h at a temperature of 573 K and 938 h at a temperature of
786 623 K, respectively. After holding at elevated temperatures, fine precipitates of approximately
787 20–50 nm were observed. During cryomilling in liquid N_2, most of the alloying elements are
788 essentially dissolved into the aluminum matrix, forming a supersaturated solid solution. Small
789 amounts of impurity elements (O, N, C, H, Fe, Cr, etc.) are also introduced into the Al alloys

790 during cryomilling, with some of them forming nanoscale dispersions [223], which can enhance
791 the retarding force on GB migration. The presence of second phases (nanoscale aluminum
792 oxides, nitrides, carbides, or precipitates), in combination with GB segregation of solute and/or
793 impurity elements is considered to play a significant role in stabilizing the microstructure.

794 Burke developed a model of grain growth based on the drag forces exerted by the dispersion
795 particles on the migrating GBs [224]. In this model, it is considered that the grain growth rate is
796 controlled by the decreasing difference between the ultimate limiting grain size and the changing
797 value of the instantaneous grain size. Burke assumed that the drag force is independent of grain
798 size, which is reasonable under the condition that the source of pinning does not depend on grain
799 size. This situation exists when pinning is produced from dispersion particles or pores. Burke's
800 model may be expressed by the following equation:

801
$$\frac{D_0 - D}{D_m} + \ln\left(\frac{D_m - D_0}{D_m - D}\right) = \frac{k_0 t}{D_m^2} \exp\left(\frac{-Q}{RT}\right) \quad (4)$$

802 where D is the average instantaneous grain size, k_0 is a constant and Q is the activation energy
803 for grain growth, t is the annealing time, and D_m is the limiting ultimate grain size for the
804 particular annealing temperature. By differentiating Eq. (4), the following growth rate equation is
805 obtained:

806
$$\frac{dD}{dt} = k\left(\frac{1}{D} - \frac{1}{D_m}\right) \quad (5)$$

807 From the linear plot of $dD/dt - 1/D$, the value of slope (k) at the different annealing
808 temperature can be determined. Using Beck's equation, the value of activation energy for grain
809 growth can be determined from the plot of $ln(k)$ as a function of $1000/RT$ [221]. From values of
810 activation energy for grain growth, two-grain growth regimes were identified: the low-

temperature region (<573 K (300°C)) and the high-temperature region (>573 K (300°C)). For temperatures lower than 573 K (300°C), the activation energy of 25 ± 5 kJ/mol was determined. This low activation energy represents the energy for the reordering of GBs in the UFG material. For temperatures higher than 573 K (300°C), the activation energy of 124 ± 5 kJ/mol was measured. This activation energy, 124 ± 5 kJ/mol, lies between that for GB diffusion and lattice diffusion in analogous Al polycrystalline systems [221].

D. Engineering Applications

A specific example of a practical application of cryomilled NC Al alloys involves target components in the U.S. Marine Corps Assault Amphibious Vehicle (AAV7A1) [225], which provides a range of services on a battlefield. The weight of an empty AAV7A1 is 21 t, and the Al hull, made from Al 5083 (Al-4.4Mg-0.7Mn-0.15Cr, UTS of 310 MPa), contributes about 14 t to this weight. Another significant proportion of the additional weight is the steel armor that is bolted on. Reducing the overall weight of the AAV7A1 is a prime objective given the need to decrease the fuel consumption. As a consequence, an important technical goal is to increase the strength of the Al 5083 while retaining its welding and anticorrosion properties, and consequently decreasing the overall amount of material required (and thereby overall weight). Similarly, improving the ballistic performance of Al 5083 will also decrease the amount of additional steel armor needed. Initial results obtained from a research program funded by the Navy suggests that these dual objectives can be achieved through the implementation of cryomilling, which can produce NC Al 5083 with a UTS greater than 700 MPa [159]. In terms of ballistics performance, the resistance of consolidated (HIP, extrusion, and rolling) cryomilled Al 5083 strip against a small-caliber, armor-piercing threat has been established and based on the test results [69], it is estimated that, a 13 mm thick cryomilled plate is equivalent to a 19 mm

standard plate, which represents 33% less weight required to stop the same threat, saving over 4.5 t on a hull weighing 14 t.

In terms of corrosion, comparison tests of consolidated cryomilled Al 5083 with standard coarse grained Al 5083 were completed to evaluate their corrosion behavior in salt-containing aqueous solutions and their susceptibility to intergranular corrosion in the nitric acid mass loss test [226]. Results show that there was not a significant difference in the corrosion behavior between the two types of materials, and that the cryomilled material exhibited less susceptibility to intergranular corrosion.

Finally, in terms of joining, tungsten inert gas welding was used to join a plate made from cryomilled materials to a standard Al 5083 plate, resulting in a weld with the same hardness as that of the standard plate. Similarly, two tubes of cryomilled Al 5083 were inertia welded together, without any drop in hardness at the weld interface [225]. The hardness of a joint of friction-stir welded cryomilled Al 5083 dropped slightly to ~125 diamond-pyramid hardness (DPH).

ACKNOWLEDGEMENTS

CCK wishes to thank NSF and DOE for support of his research on this topic under grants number DMR-1401725 and DE-0000538 respectively. EJL is grateful for the funding provided by the Office of Naval Research that supported the work by his group reviewed in this article: Grant No. ONR N00014-12-1-0237 under the guidance of Dr. Larry Kabacoff and Grant No. N00014-12-C-0241 under the guidance of Rod Peterson and Bill Golumbfskie. The work of TGL was supported by the U.S. National Science Foundation under Grant No. DMR-1160966.

REFERENCES

1. H. Gleiter, Progress in Materials Science, (1989) **33**, 223-315.
2. U. Erb, K. T. Aust, G. Palumbo, Chapter 6 in Nanostructured Materials, Processing, Properties, andApplications, 2nd edition, ed. C. C. Koch, William Andrew, Norwich, NY 2007.
3. Y. Yoshizawa, S. Oguma, K. J. Yamauchi, J. Appl. Phys.(1988) **64**, 6044.
4. R. Z. Valiev, R. K. Ishamgaliev, I. V. Alexandrov, Prog. Mater. Sci. (2000) **45**, 103.
5. J. R. Groza and R. J. Dowding, NanoStructured Materials, (1996) **7,** 749.
6. S. Yu, C-J. Sun, G-M. Chow, Chapter 1 in Nanostructured Materials, Processing, Properties , and Applications, 2nd edition, ed. C. C. Koch, William Andrew, Norwich, NY, 2007.
7. R.Z. Valiev, Y. Estrin, Z. Horita, T.G. Langdon, M.J. Zehetbauer, and Y.T. Zhu: *JOM*, 2006, vol. 58 (4), pp. 33-39.
8. J.T. Wang: *Mater. Sci. Forum*, 2006, vol. 503-504, pp. 363-370.
9. T.G. Langdon: *Mater. Sci. Forum*, 2011, vol. 667-669, pp. 9-14.
10. S. Srinivasan and S. Ranganathan: *India's Legendary Wootz Steel: An Advanced Material of the Ancient World*, National Institute of Advanced Studies and IISc, Bangalore, India, 2004.
11. O.D. Sherby and J. Wadsworth: *J. Mater. Proc. Technol.*, 2001, vol. 117. pp. 347-363.
12. P.W. Bridgman: *Phys. Rev.*, 1935, vol. 48, pp. 825-847.
13. P.W. Bridgman: *Studies in Large Scale Plastic Flow and Fracture*, McGraw-Hill, New York, NY, U.S.A., 1952.
14. K. Edalati and Z. Horita: *Mater. Sci. Eng. A*, 2016, vol. A652, pp. 325-352.
15. N.A. Smirnova, V.I. Levit, V.I. Pilyugin, R.I. Kuznetsov, L.S. Davydova, and V.A. Sazonova: *Fiz. Metal. Metalloved.*, 1986, vol. 61, pp. 1170-1177.
16. V.M. Segal, V.I. Reznikov, A.E. Drobyshevskiy, and V.I. Kopylov: *Russian Metal.*, 1981, vol. 1, pp. 99-105.
17. R.Z. Valiev, O.A. Kaibyshev, R.I. Kuznetsov, R.Sh. Musalimov, and N.K. Tsenev: *Dokl. Akad. Nauk SSSR*, 1988, vol. 301, pp. 864-866.
18. T.G. Langdon: *Int. J. Mater. Res*., 2007, vol. 98, pp. 251-254.
19. R.Z. Valiev, N.A. Krasilnikov, and N.K. Tsenev: *Mater. Sci. Eng. A*, 1991, vol. A137, pp. 35-40.
20. R.Z. Valiev, A.V. Korznikov, and R.R. Mulyukov: *Mater. Sci. Eng. A*, 1993, vol. A168, pp. 141-148.
21. Y. Saito, N. Tsuji, H. Utsunomiya, T. Sakai, and R.G. Hong: *Scr. Mater.*, 1998, vol. 39, pp. 1221-1227.
22. Y. Saito, H. Utsunomiya, N. Tsuji, and T. Sakai: *Acta Mater.*, 1999, vol. 47, pp. 579-583.
23. O.R. Valiakhmetov, R.M. Galeyev, and G.A. Salishchev: *Fiz. Metall. Metalloved,* 1990, vol. 10, pp. 204-206.
24. S.V. Zherebtsov, G.A. Salishchev, R.M. Galeyev, O.R. Valiakhmetov, S.Yu. Mironov and S.L. Semiatin: *Scripta Mater*., 2004, vol. 51, pp. 1147-1151.
25. B. Cherukuri, T.S. Nedkova, and R. Srinivasan: *Mater. Sci. Eng.* A, 2005, vol. A410-411, pp. 394-397.

902 26. A. Kundu, R. Kapoor, R. Tewari, and J.K. Chakravarty: *Scr. Mater.*, 2008, vol. 58, pp.
903 235-238.
904 27. J. Richert and M. Richert: *Aluminium*, 1986, vol. 62, pp. 604-609.
905 28. M. Richert, H.P. Stüwe, M.J. Zehetbauer, J. Richert, R. Pippan, Ch. Motz, and E. Schafler:
906 *Mater. Sci. Eng.A*, 2003, vol. A355, pp. 180-185.
907 29. Y.T. Zhu, H.G. Jiang, J.Y. Huang, and T.C. Lowe: *Metall. Mater. Trans.,* 32A (2001), pp.
908 1559-1562.
909 30. J.Y. Huang, Y.T. Zhu, H.G. Jiang, and T.C. Lowe : *Acta Mater.,* 49 (2001), pp. 1497-1501.
910 31. Y. Beygelzimer, D. Orlov, and V. Varyukhin: *Ultrafine Grained Materials II*, ed. Y.T.
911 Zhu, T.G. Langdon, R.S. Mishra, S.L. Semiatin, M.J. Saran, T.C. Lowe, TMS, Warrendale,
912 PA, pp. 297-304 (2002).
913 32. V. Varyukhin, Y. Beygelzimer, S. Synkov, and D. Orlov: *Mater. Sci. Forum*, 2006, vol.
914 503-504, pp. 335-340.
915 33. T.G. Langdon: *Acta Mater.* 2013, vol. 61, pp. 7035-7059.
916 34. A.P. Zhilyaev, S. Lee, G.V. Nurislamova, R.Z. Valiev, and T.G. Langdon: *Scr. Mater.*,
917 2001, vol. 44, pp. 2753-2758.
918 35. A.P. Zhilyaev, G.V. Nurislamova, B.K. Kim, M.D. Baró. J.A. Szpunar, and T.G. Langdon:
919 *Acta Mater.*, 2003, vol. 51, pp. 753-765.
920 36. J. Wongsa-Ngam, M. Kawasaki, and T.G. Langdon: *J. Mater. Sci.*, 2013, vol. 48, pp. 4653-
921 4660.
922 37. X.C. Xu, Q. Zhang, N. Hu, Y. Huang, and T.G. Langdon: *Mater. Sci. Eng. A*, 2013, vol.
923 A588, pp. 280-287.
924 38. P.M. Bhovi, D.C. Patil, S.A. Kori, K. Venkateswarlu, Y. Huang, and T.G. Langdon: *J.*
925 *Mater. Res. Tech.*, 2016, vol. 5, pp. 353-359.
926 39. R.Z. Valiev and T.G. Langdon: *Prog. Mater. Sci.*, 2006, vol. 51, pp. 881-981.
927 40. Y. Iwahashi, J. Wang, Z. Horita, M. Nemoto, and T.G. Langdon: *Scr. Mater.*, 1996, vol.
928 35, pp. 143-146.
929 41. M. Furukawa, Z. Horita, Y. Iwahashi, M. Nemoto, and T.G. Langdon: *Mater. Sci. Eng. A*,
930 1998, vol. A257, pp. 328-332.
931 42. Y. Iwahashi, Z. Horita, M. Nemoto, and T.G. Langdon: *Acta Mater.*, 1997, vol. 45, pp.
932 4733-4741.
933 43. Y. Iwahashi, Z. Horita, M. Nemoto, and T.G. Langdon: *Acta Mater.*, 1998, vol. 46, pp.
934 3317-3331.
935 44. M. Kawasaki, Z. Horita, and T.G. Langdon: *Mater. Sci. Eng. A*, 2009, vol. A524, pp. 143-
936 150.
937 45. C. Xu, M. Furukawa, Z. Horita, and T.G. Langdon: *Mater. Sci. Eng. A*, 2005, vol. A398,
938 pp. 66-76.
939 46. M. Prell, C. Xu, and T.G. Langdon: *Mater. Sci. Eng. A*, 2008, vol. A480, pp. 449-455.
940 47. C. Xu, Z. Horita, and T.G. Langdon: *Mater. Sci. Eng. A*, 2011, vol. A528, pp. 6059-6065.
941 48. A.P. Zhilyaev and T.G. Langdon: *Prog. Mater. Sci.*, 2008, vol. 53, pp. 893-979.
942 49. R.Z. Valiev, Yu.V. Ivanisenko, E.F. Rauch, and B. Baudelet: *Acta Mater.*, 1996, vol. 44,
943 pp. 4705-4712.
944 50. F. Wetscher, A. Vorhauer, R. Stock, and R. Pippan: *Mater. Sci. Eng. A*, 2004, vol. 387-389,
945 pp. 809-816.
946 51. C. Xu, Z. Horita, and T.G. Langdon: *Acta Mater.*, 2007, vol. 55, pp. 203-212.
947 52. C. Xu, Z. Horita, and T.G. Langdon: *Acta Mater.*, 2008, vol. 56, pp. 5168-5176.

53. Y. Estrin, A. Molotnikov, C.H.J. Davies, and R. Lapovok: *J. Mech. Phys. Solids*, 2008, vol. 56, pp. 1186-1202.
54. M. Kawasaki, R.B. Figueiredo, and T.G. Langdon: *Acta Mater.*, 2011, vol. 59, pp. 308-316.
55. M. Kawasaki, B. Ahn, and T.G. Langdon: *Mater. Sci. Eng. A*, 2010, vol. A527, pp. 7008-7016.
56. M. Kawasaki: *J. Mater. Sci.*, 2014, vol. 49, pp. 18-34.
57. J. Wongsa-Ngam and T.G. Langdon: *Mater. Sci. Forum*, 2014, vol. 783-786, pp. 2635-2640.
58. R.Z. Valiev and T.G. Langdon: *Adv. Eng. Mater.*, 2010, vol. 12, pp. 677-691.
59. R.Z. Valiev and T.G. Langdon: *Metall. Mater. Trans. A*, 2011, vol. 42A, pp. 2942-2951.
60. R.Z. Valiev, I. Sabirov, A.P. Zhilyaev, and T.G. Langdon: *JOM*, 2012, vol. 64, pp. 1134-1142.
61. K. Nakashima, Z. Horita, M. Nemoto, and T.G. Langdon: *Mater. Sci. Eng. A*, 2000, vol. A281, pp. 82–87.
62. G.I. Raab: *Mater. Sci. Eng. A*, 2005, vol. 410-411, pp. 230-233.
63. M.Yu. Murashkin, E.V. Bobruk, A.R. Kil'mametov, and R.Z. Valiev: *Phys. Metals Metallog.*, 2009, vol. 108, pp. 415-423.
64. R.Z. Valiev, M.Yu. Murashkin, E.V. Bobruk, and G.I. Raab: *Mater. Trans.*, 2009, vol. 50, pp. 87-91.
65. I. Sabirov, M.T. Perez-Prado, M. Murashkin, J.M. Molina-Aldareguia, E.V. Bobruk, N.F. Yunusova, and R.Z. Valiev: *Int. J. Mater. Form.*, 2010, vol. 3 (suppl. 1), pp. 411-414.
66. D. Green: *J. Inst. Metals*, 1972, vol. 100, pp. 295-300.
67. C. Etherington: *J. Eng. Ind.*, 1974, vol. 96, pp. 893-900.
68. G.J. Raab, R.Z. Valiev, T.C. Lowe, and Y.T. Zhu: *Mater. Sci. Eng. A*, 2005, vol. A382, pp. 30-34.
69. G.I. Raab, R.Z. Valiev, D.V. Gunderov, T.C. Lowe, A. Misra, and Y.T. Zhu: *Mater. Sci. Forum*, 2008, vol. 584-586, pp. 80-85.
70. S. Katsas, R. Dashwood, G. Todd, M. Jackson, and R. Grimes: *J. Mater. Sci.*, 2010, vol. 45, pp. 4188-4195.
71. V.M. Segal: *J. Mater. Process. Tech.*, 2010, vol. 210, pp. 542-549.
72. C. Xu, S. Schroeder, P.B. Berbon, and T.G. Langdon: *Acta Mater.*, 2010, vol. 58, pp. 1379-1386.
73. A.V. Polyakov, I.P. Semenova, G.I. Raab, V.D. Sitdikov, and R.Z. Valiev: *Rev. Adv. Mater. Sci.*, 2012, vol. 31, pp. 78-84.
74. I.P. Semenova, A.V. Polyakov, G.I. Raab, T.C. Lowe, and R.Z. Valiev: *J. Mater. Sci.*, 2012, vol. 47, pp. 7777-7781.
75. D.V. Gunderov, A.V. Polyakov, I.P. Semenova, G.I. Raab, A.A. Churakova, E.I. Gimaltdinova, I. Sabirov, J. Segurado, V.D. Sitdikov, I.V. Alexandrov, N.A. Enikeev, and R.Z. Valiev: *Mater. Sci. Eng. A*, 2013, vol. A562, 128-136.
76. J.T. Wang, Z. Li, J. Wang, and T.G. Langdon: *Scr. Mater.*, 2012, vol. 67, pp. 810-813.
77. P.W. Bridgman: *J. Appl. Phys.*, 1943, vol. 14, pp. 273-283.
78. Z. Li, P.F. Zhang, H. Yuan, K. Lin, Y. Liu, D.L. Yin, J.T. Wang, and T.G. Langdon: *Mater. Sci. Eng. A*, 2016, vol. A658, pp. 367-375.
79. T.H. Fang, W.L. Li, N.R. Tao, and K. Lu: *Science*, 2011, vol. 331, pp. 1587-1590.
80. X. Wu, P. Jiang, L. Chen, F. Yuan, and Y.T. Zhu: *Proc. Natl. Acad. Sci. USA*, 2014, vol. 111, pp. 7197-7201.

81. K. Lu: *Science*, 2014, vol. 345, pp. 1455-1456.
82. W. Wang, F. Yuan, and X. Wu, *Comput. Mater. Sci.*, 2015, vol. 110, pp. 83-90.
83. A.V. Korznikov, I.M. Safarov, D.V. Laptionok, and R.Z. Valiev: *Acta Metall. Mater.*, 1991, vol. 39, pp. 3193-3197.
84. H. Shen, B. Guenther, A.V. Korznikov, and R.Z. Valiev: *Nanostruct. Mater.*, 1995, vol. 6, pp. 385-388.
85. R.Z. Valiev, R.S. Mishra, J. Groza, and A.K. Mukherjee: *Scr. Mater.*, 1996, vol. 34, pp. 1443-1448.
86. J. Sort, A.P. Zhilyaev, M. Zielinska, J. Nogues, S. Suriñach, J. Thibault, and M.D. Baró: *Acta Mater.*, 2003, vol. 51, pp. 6385-6393.
87. Z. Lee, F. Zhou, R.Z. Valiev, E.J. Lavernia, and S.R. Nutt: *Scr. Mater.*, 2004, vol. 51, pp. 209-214.
88. K.V. Rajulapati, R.O. Scattergood, K.L. Murty, Z. Horita, T.G. Langdon, and C.C. Koch: *Metall. Mater. Trans. A*, 2008, vol. 39A, pp. 2528-2534.
89. K. Kaneko, T. Hata, T. Tokunaga, and Z. Horita: *Mater. Trans.*, 2009, vol. 50, pp. 76-81.
90. K. Edalati, Z. Horita, H. Fujiwara, and K. Ameyama: *Metall. Mater. Trans. A*, 2010, vol. A41, pp. 3308-3317.
91. K. Edalati, S. Toh, M. Watanabe, and Z. Horita: *Acta Mater.*, 2012, vol. 60, pp. 3885-3893.
92. K. Edalati, S. Toh, M. Watanabe, and Z. Horita: *Scr. Mater.*, 2012, vol. 66, pp. 386-389.
93. K. Edalati, S. Toh, H. Iwaoka, M. Watanabe, Z. Horita, D. Dashioka, K. Kishida, and H. Inui: *Scr. Mater.*, 2012, vol. 67, pp. 814-817.
94. J.M. Cubero-Sesin and Z. Horita: *Mater. Sci. Eng. A*, 2012, vol. A558, pp. 462-471.
95. P. Jenei, J. Gibicza, E.Y. Yoon, and H.S. Kim: *J. Alloys Compd.*, 2012, vol. 539, pp. 32-36.
96. E.Y. Yoon, D.J. Lee, T.S. Kim, H.J. Chae, P. Jenei, J. Gubicza, T. Ungár, M. Janecek, J. Vratna, S. Lee, and H.S. Kim: *J. Mater. Sci.*, 2012, vol. 47, pp. 7117-7123.
97. A.P. Zhilyaev, G. Ringot, Y. Huang, J.M. Cabrera, and T.G. Langdon: *Mater. Sci. Eng. A*, 2017 (in press).
98. E. Menéndez, J. Sort, V. Langlais, A. Zhilyaev, J.S. Muñoz, S. Suriñach, J. Nogués, and M.D. Baró: *J. Alloys Compd.*, 2007, vol. 434-435, pp. 505-508.
99. E. Menéndez, G. Salazar-Alvarez, A.P. Zhilyaev, S. Suriñach, M.D. Baró, J. Nogués, and J. Sort: *Adv. Funct. Mater.*, 2008, vol. 18, pp. 3293-3298.
100. H. Li, A. Misra, Y. Zhu, C.C. Koch, and T.G. Holesinger: *Mater, Sci. Eng. A*, 2009, vol. A523, pp. 60-64.
101. H. Li, A. Misra, Z. Horita, C.C. Koch, N.A. Mara, P.O. Dickerson, and Y. Zhu: *J. Appl. Phys.*, 2009, vol. 95, pp. 071907(1-4).
102. A. Bachmaier, A. Hohenwarter, and R. Pippan: *Scr. Mater.*, 2009, vol. 61, 1016-1019.
103. J. Sort, D.C. Ile, A.P. Zhilyaev, A. Concustell, T. Czeppe, M. Stoica, S. Suriñach, J. Eckert, and M.D. Baró: *Scr. Mater.*, 2004, vol. 50, pp. 1221-1225.
104. A.R. Yavari, W.J. Botta, C.A.D. Rodrigues, C. Cardoso, and R.Z. Valiev: *Scr. Mater.*, 2002, vol. 46, pp. 711-716.
105. Z. Kovács, P. Henits, A.P. Zhilyaev, and A. Révész: *Scr. Mater.*, 2006, vol. 54, pp. 1733-1737.
106. N. Boucharat, R. Hebert, H. Rösner, R.Z. Valiev, and G. Wilde: *J. Alloys Compds.,* 2007, vol. 434-435, pp. 252-254.
107. T. Czeppe, G. Korznikova, J. Morgiel, A. Korznikov, N.Q. Chinh, P. Ochin, and A. Sypien *J. Alloys Compds*., 2009, vol. 483, pp. 74-77.

108. A.P. Zhilyaev, A.A. Gimazov, G.I. Raab, and T.G. Langdon: *Mater. Sci. Eng. A*, 2008, vol. A486, pp. 123-128.
109. A.P. Zhilyaev, S. Swaminathan, A.A. Gimazov, T.R. McNelley, and T.G. Langdon: *J. Mater. Sci.*, 2008, vol. 43, pp. 7451-7456.
110. K. Edalati, Y. Yokoyama, and Z. Horita: *Mater. Trans.*, 2010, vol. 51, pp. 23-26.
111. K. Edalati and Z. Horita: *Scr. Mater.*, 2010, vol. 63, pp. 174-177.
112. M.C. Chen, H.C. Hsieh, and W. Wu: *J. Alloys Compds.*, 2006, vol. 416, pp. 169-172.
113. M.C. Chen, C.W. Kuo, C.M. Chang, C.C. Hsieh, Y.Y. Chang, and W. Wu: *Mater. Trans.*, 2007, vol. 48, pp. 2595-2598.
114. M. Eizadjou, A.K. Talachi, H.D. Manesh, H.S. Shahabi, and K. Janghorban: *Compos. Sci. Technol.*, 2008, vol. 68, pp. 2003-2009.
115. R.N. Dehsorkhi, F. Qods, M. Tajally *Mater. Sci. Eng. A*, 2011, vol. A530, pp. 61-72.
116. N. Chang, M.Y. Zheng, C. Xu, G.D. Fan, H.G. Brokmeier, and K. Wu: *Mater. Sci. Eng. A*, 2012, vol. A543, pp. 249-256.
117. B. Beausir, J. Scharnweber, J. Jaschinski, H.G. Brokmeier, C.G. Oertel, W. Skrotzki: *Mater. Sci. Eng. A*, 2010, vol. A527, pp. 3271-3278.
118. K. Oh-ishi, K. Edalati, H.S. Kim, K. Hono, and Z. Horita: *Acta Mater.*, 2013, vol. 61, pp. 3482-3489.
119. O. Bouaziz, H.S. Kim, and Y. Estrin: *Adv. Eng. Mater.*, 2013, vol. 15, pp. 336-340.
120. B. Ahn, A.P. Zhilyaev, H.J. Lee, M. Kawasaki, and T.G. Langdon: *Mater. Sci. Eng. A*, 2015, vol. A635, pp. 109-117.
121. M. Kawasaki, B. Ahn, H.J. Lee, A.P. Zhilyaev, and T.G. Langdon: *J. Mater. Res.*, 2016, vol. 31, pp. 88-99.
122. B. Ahn, H.J. Lee, I.C. Choi, M. Kawasaki, J.I. Jang, and T.G. Langdon: *Adv. Eng. Mater.*, 2016, vol. 18, pp. 1001-1008.
123. M. Kawasaki, B. Ahn, P. Kumar, J.I. Jang, and T.G. Langdon: *Adv. Eng. Mater.*, 2017, vol. 19, pp. 1600578(1-17).
124. R.B. Figueiredo, P.R. Cetlin, and T.G. Langdon: *Mater. Sci. Eng. A*, 2011, vol. A528, pp. 8198-8204.
125. R.B. Figueiredo, P.H.R. Pereira, M.T.P. Aguilar, P.R. Cetlin, and T.G. Langdon: *Acta Mater.*, 2012, vol. 60, pp. 3190-3198.
126. M. Kawasaki, S.N. Alhajeri, C. Xu, and T.G. Langdon: *Mater. Sci. Eng. A*, 2011, vol. A529, pp. 345-351.
127. H.J. Lee, S.K. Lee, K.H. Jung, G.A. Lee, B. Ahn, M. Kawasaki, and T.G. Langdon: *Mater. Sci. Eng. A*, 2015, vol. A630, pp. 90-98.
128. K. Lu: *Science*, 2010, vol. 328, pp. 319-320.
129. R. Birringer: *Mater. Sci. Eng. A*, 1989, vol. A117, pp. 33-43.
130. B. Gunther, A. Kumpmann, and H.-D. Kunze: *Scripta Metall. Mater.*1992, vol.27, pp. 833-838.
131. M. Ames, J. Markmann, R. Karos, A. Michels, A. Tschope, and R. Birringer: *Acta Mater.* 2008, vol. 56, pp. 4255-4266.
132. F. J. Humphreys, and M. Hatherly: Recrystallization and Related Annealing Phenomena, chapter 9, (Elsevier Science, Inc., Tarrytown, NY, 1996), pp. 289-295.
133. C. E. Krill, H. Ehrhardt, and R. Birringer: *Z. Metallkd.* 2005, vol. 96, pp. 1134-1141
134. J. W. Cahn: *Acta Metallurgica*, 1962, vol.10, pp. 768-798.

135. K. Lücke, and H. P. Stüwe: *Acta Metallurgica***,** 1971, vol.19, pp. 1087-1099.
136. P. Knauth, A. Charai, and P. Gas: *Scripta Metall. Mater.* **,** 1993, vol.28, pp. 325-330.
137. A. Michels, C. E. Krill, H. Ehrhardt, R. Birringer, and D. T. Wu: *Acta Mater.*, 1999, vol.47, pp. 2143-2152.
138. R. D. Doherty, *Mater. Sci. Forum*, 2012, vol. 715, pp. 1-12.
139. R. J. Perez, H. G. Jiang, C. P. Dogan, and E. J. Lavernia: *Metall. Mater. Trans. A*, 1998, vol.29A, pp. 2469-2475.
140. H. J. Hofler, and R. S. Averback: *Scripta Metall. Mater.*, 1990, vol. 24, pp. 2401-2406.
141. Z. Gao, and G. Fultz: *NanoStructured Mater.*, 1994, vol. 4, pp. 939-947.
142 Y. Estrin, G. Gottstein, E. Rabkin, and L. S. Shvindlerman: *Scripta Mater.*, 2000, vol. 43, pp. 141-147.
143. E. D. Hondros, and M. P. Seah: in *Physical Metallurgy*, 3rd edition, ed. R. W. Cahn and P. Haasen, Elsevier Sci. Publ. BV, (1983) p. 856.
144. J. Weissmuller: *NanoStructured Mater.*, 1993, vol. 3, pp. 261-272, & *J. Mater. Res.*, 1994, vol. 9, pp. 4-7.
145. R. Kirchheim: *Acta Mater.*, 2002, vol. 50, pp. 413-419.
146. J. R. Trelewicz, and C. A. Schuh: *Phys. Rev. B*, 2009, vol. 79, p. 094112.
147. M. Saber, H. Kotan, C. C. Koch, and R. O. Scattergood: *J. Appl. Phys.*, 2013, vol. 113 p. 063515.
148. P. Wynblatt, and R. C. Ku: *Surf. Sci.* 1977, vol. 65, pp. 511-531.
149. T. Chookajorn, H. A. Murdoch, and C. A. Schuh: *Science*, 2012, vol. 337, pp. 951-954.
150. A. R. Kalidindi, T. Chookajorn, and C. A. Schuh: *JOM,* 2015, vol. 67, pp. 2834-2843.
151. S. J. Dillon, M. Tang, W. C. Carter, and M. P. Harmer: *Acta Mater.,* 2007, vol. 55, pp. 6208-6218.
152. T. J. Rupert: *Current Opinion in Solid State and Mater. Sci.*, 2016, vol. 20, pp. 257-267.
153. A. Khalajhedayati, and T. J. Rupert: *JOM,* 2015, vol. 67, pp. 2788-2801.
154. M. Saber, H. Kotan, C. C. Koch, and R. O. Scattergood: *Mater. Sci. Engr. A*, 2012, vol. 556**,** pp. 664-670.
155. L. Li, M. Saber, W. Xu, Y. Zhu, C. C. Koch, and R.O. Scattergood: *Mater. Sci. Engr. A*, 2014, vol. 613, pp. 289–295.
156. M. Saber, H. Kotan, C. C. Koch, and R.O. Scattergood: *J. Appl. Phys.*, 2013, vol.114, p. 103510.
157. E.J. Lavernia, B.Q. Han, and J.M. Schoenung: *Mater. Sci. Eng. A,* 2008, vol. 493, pp. 207-214.
158. H.J. Fecht: *Nanophase Materials: Synthesis, Properties, Applications*, in: G.C. Hadjipanayis, R.W. Siegel (Eds.), Kluwer Academic, Dordrecht, Netherlands, 1994.
159. D.B. Witkin, and E.J. Lavernia: *Prog. Mater. Sci.*, 2006, vol. 51, pp. 1-60.
160. J.A. Picas, A. Forn, L. Ajdelsztajn, and J. Schoenung: *Powder Tech.*, 2004, vol. 148, pp. 20-23.
161. B. Huang, R.J. Perez, and E.J. Lavernia: *Mater. Sci. Eng. A*, 1998, vol. 255, pp. 124-132.
162. O. Ertorer, T. Topping, Y. Li, W. Moss, and E.J. Lavernia: *Scripta Mater.*, 2009, vol. 60, pp. 586-589.

163. X. Zhang, H. Wang, R.O. Scattergood, J. Narayan, and C.C. Koch: *Acta Mater.*, 2002, vol. 50, pp. 3995-4004.
164. B. Zheng, O. Ertorer, Y. Li, Y. Zhou, S. N. Mathaudhu, C. Y.A. Tsao, and E.J. Lavernia: *Mater. Sci. Eng. A*, 2011, vol. 528, pp. 2180-2191.
165. B. Zheng , Y. Li , W. Xu , Y. Zhou , S.N. Mathaudhu , Y. Zhu, and E.J. Lavernia, *Phil. Mag. Lett.*, 2013, vol. 93, pp. 457-464.
166. N. Yang, J.K. Yee, Z. Zhang, L. Kurmanaeva, P. Cappillino, V. Stavila, E.J. Lavernia, and C. San Marchi: *Acta Mater.*, 2015, vol. 82, pp. 41-50.
167. K.M. Youssef, A.J. Zaddach, C. Niu, D.L. Irving, and C.C. Koch: *Mater. Res. Lett.*, 2015, vol. 3, pp. 95-99.
168. B. Zheng, Z. Fu, L. Kurmanaeva, Y. Lin, J. Ivanisenko, Y. Zhou, F. Chen, H. Hahn, L. Zhang, and E.J. Lavernia: *TMS2016*, Nashville TN, 2016.
169. J. Ye, J. He, and J.M. Schoenung: *Metall. Mater. Trans. A*, 2006, vol. 37, pp. 3099-3109.
170. F. Tang, M. Hagiwara, and J.M. Schoenung: *Scripta Mater.*, 2005, vol. 53, pp. 619-624.
171. H.-J. Fecht: *Nanostruct. Mater.*, 1995, vol. 6, pp. 33-42.
172. F. Zhou, X.Z. Liao, Y.T. Zhu, S. Dallek, and E.J. Lavernia: *Acta Mater.*, 2003, vol. 51, pp. 2777-2791.
173. X.Z. Liao, J.Y. Huang, Y.T. Zhu, F. Zhou, and E.J. Lavernia: *Phil. Mag.*, 2003, vol. A83, pp. 3065-3075.
174. J. Eckert, J.C. Holzer, C.E. Krill III, and W.L. Johnson: *J. Mater. Res.*, 1992, vol. 7, pp. 1751-1761.
175. F.A. Mohamed: *Acta Mater.*, 2003, vol. 51, pp. 4107-4119.
176. B. Zheng, D. Zhang, Y. Zhou, S.N. Mathaudhu, and E.J. Lavernia: in D.C.a.R.M. Gasior (Ed.) *Adv. in Powder Metall. & Particulate Mater. 2013*, Metal Powder Industries Federation, Chicago, IL, 2013.
177. D.T.A. Matthews, V. Ocelík, P.M. Bronsveld, and J.T.M. De Hosson: *Acta Mater.*, 2008, vol. 56, pp. 1762-1773.
178. K. Hajlaoui, A.R. Yavari, B. Doisneau, A. LeMoulec, W.J. Botta F,G. Vaughan, A.L. Greer, A. Inoue, W. Zhang, and Å. Kvick: *Scripta Mater.*, 2006, vol. 54, pp. 1829-1834.
179. X. Zhang, H. Wang, and C.C. Koch: *Rev. Adv. Mater. Sci.*, 2004, vol. 6, pp. 53-93.
180. K.H. Chung, D.H.S. J. He, and J.M. Schoenung: *Mater. Sci. Eng. A*, 2003, vol. 356, pp. 23-31.
181. R. Vogt, Z. Zhang, Y. Li, M. Bonds, N.D. Browning, E.J. Lavernia, and J.M. Schoenung: *Scripta Mater.*, 2009, vol. 61, pp. 1052-1055.
182. C.C. Koch: in H. R.W. Siegel , M.C. Roco (Ed.) Final report by WTEC panel, 1999, pp. 93.
183. Y.T. Zhu, and X. Liao: *Nature Mater.*, 2004, vol. 3, pp. 351-352.
184. L. Lu, Y.F. Shen, X.H. Chen, L.H. Qian, and K. Lu: *Science*, 2004, vol. 304, pp. 422-426.
185. Y.H. Zhao, J.F. Bingert, X.Z. Liao, B.Z. Cui, K. Han, A.V. Sergueeva, A.K. Mukherjee, R.Z. Valiev, T.G. Langdon, and Y.T. Zhu: *Adv. Mater.*, 2006, vol. 18, pp. 2949-2953.
186. K. Lu, *Nature Rev. Mater.*, 2016, vol. 1, #16019, pp. 1-13.
187. L. Lu, Y.F. Shen, X.H. Chen, L.H. Qian, and K. Lu: *Science*, 2004, vol. 304, pp. 422-426.
188 M.A. Meyers, O. Vohringer, and V.A. Lubarda: *Acta Mater.*, 2001, vol. 49, pp. 4025-4039.
189. M.A. Meyers, A. Mishra, and D.J. Benson: *Prog. Mater. Sci.*, 2006, vol. 51, pp. 427-556.

190. E. El-Danaf, S.R. Kalidindi, and R.D. Doherty: *Metall. Mater. Trans. A*, 1999, vol. 30, pp. 1223-1233.
191. Y.T. Zhu, X.Z. Liao, and X.L. Wu: *Prog. Mater. Sci.*, 2012, vol. 57, pp. 1-62.
192. B. Zheng , Y. Li , W. Xu , Y. Zhou , S.N. Mathaudhu , Y. Zhu, and E.J. Lavernia, Phil. Mag. Let., 2013, vol. 93, pp. 457-464.
193. J. He, K.H. Chung, X.Z. Liao, Y.T. Zhu, and E.J. Lavernia: *Metall. Mater. Trans. A*, 2003, vol. 34A, pp. 707-712.
194. S. Mahajan, and G.Y. Chin: *Acta Mater*, 1973, vol. 21, pp. 1353-1363.
195. W.B. Jones, and H.I. Dawson: in R.W. Rohde, B.M. Butcher, J.R. Holland, C.H. Karnes (Eds.) *Metallurgical Effects at High Strain Rates*, Plenum Press, New York, NY,, 1973, pp. 443-459.
196. V. Yamakov, D. Wolf, S.R. Phillpot, A.K. Mukherjee, and H. Gleiter: *Nature Mater.*, 2002, vol. 1, pp. 45-49.
197. J.A. Venables: in R.E. Reed-Hill, J. P. Hirth, H.C. Rogers (Eds.) *Deformation Twinning*, Gordon & Breach, NY, 1964, pp. 77-116.
198. K.W. Jacobsen, and J. Schiøtz: *Nature Mater.*, 2002, vol. 1, pp. 15-16.
199. Y. Wang, L.Q. Chen, Z.K. Liu, and S.N. Mathaudhu: *Scripta Mater.*, 2010, vol. 62, pp. 646-649.
200. H. Somekawa, K. Hirai, H. Watanabe, Y. Takigawa, and K. Higashi: *Mater. Sci. Eng. A*, 2005, vol. 407, pp. 53-61.
201. F. Zhou, X.Z. Liao, Y.T. Zhu, S. Dallek, and E.J. Lavernia: *Acta Mater.*, 2003, vol. 51, pp. 2777-2791.
202. F. Louchet, L.P. Kubin, and D. Vesely: *Phil. Mag. A*, 1979, vol. 39, pp. 433-454.
203. J.L. Sun, P.W. Trimby, X. Si, X.Z. Liao, N.R. Tao, and J.T. Wang: *Scripta Mater.*, 2013, vol. 68, pp. 475-478.
204. J.W. Christian, and S. Mahajant: *Prog. Mater. Sci.*, 1995, vol. 39, pp. 1-157.
205. X.L. Wu, K.M. Youssef, C.C. Koch, S.N. Mathaudhu, L.J. Kecskes, and Y.T. Zhu: *Scripta Mater.*, 2011, vol. 64, pp. 213-216.
206. M. Pozuelo, C. Melnyk, W.H. Kao, and J.-M. Yang: *J. Mater. Res.*, 2011, vol. 26, pp. 904-911.
207. Y. Li, Y.J. Lin, Y.H. Xiong, J.M. Schoenung, and E.J. Lavernia: *Scripta Mater.*, 2011, vol. 64, pp. 133-136.
208. S.N. Mathaudhu, J. Taek-Im, R.E. Barber, I.E. Anderson, I. Karaman, K.T. Hartwig, *Mater. Res. Soc. Symp. Proc.*, 2003, vol. 754, pp. CC3.5.1-8.
209. Y. Lin, and E.J. Lavernia: *Metall. Mater. Trans. A*, 2006, vol. 37, pp. 3317-3322.
210. H. Wen, Y.H. Zhao, Y. Li, O. Ertorer, K.M. Nesterov, R.K. Islamgaliev, R.Z. Valiev, and E.J. Lavernia: *Phil. Mag.*, 2010, vol. 90, pp. 4541-4550.
211. Y. Li, Y. H. Zhao, W. Liu, Z. H. Zhang, R. G. Vogt, E. J. Lavernia, and J.M. Schoenung: *Phil. Mag.*, 2010, vol. 90, pp. 783-792.
212. C.C. Koch, *J. Mater. Sci.*, 2007, vol. 42, pp. 1403-1414.
213. C. Koch, R. Scattergood, K. Darling, and J. Semones: *J. Mater. Sci.*, 2008, vol. 43, pp. 7264-7272.
214. P.V. Liddicoat, X. Liao, Y. Zhao, Y. Zhu, M.Y. Murashkin, E.J. Lavernia, R.Z. Valiev, and S.P. Ringer: *Nature Commun.*, 2010, vol. 7, pp. 1-7.
215. N. Zhou, T. Hu, J. Huang, and J. Luo: *Scripta Mater.*, 2016, vol. 124, pp. 160-163.

216. Y. Lin, H. Wen, Y. Li, B. Wen, W. Liu, and E.J. Lavernia: *Acta Mater.*, 2015, vol. 82, pp. 304-315.
217. B.J.M. Aikin, R.M. Dickerson, D.T. Jayne, S. Farmer, and J.D. Whittenberger: *Scripta Metall. Mater.*, 1994, vol. 30, pp. 119-122.
218. R.W. Hayes, P.B. Berbon, and R.S. Mishra: *Metall. Mater. Trans. A,* 2004, vol. 35, pp. 3855-3861.
219. Y. Li, W. Liu, V. Ortalan, W.F. Li, Z. Zhang, R. Vogt, N.D. Browning, E.J. Lavernia, and J.M. Schoenung: *Acta Mater.*, 2010, vol. 58, pp. 1732-1740.
220. F. Zhou, J. Lee, S. Dallek, and E.J. Lavernia: *J. Mater. Res.*, 2001, vol. 16, pp. 3451-3458.
221. I. Roy, M. Chauhan, F.A. Mohamed, and E.J. Lavernia: *Metall. Mater. Trans. A*, 2006, vol. 37, pp. 721–730.
222. B.Q. Han, Z. Zhang, and E.J. Lavernia: *Phil. Mag. Lett.*, 2005, vol. 85, pp. 97-108.
223. V.L.Tellkamp, A. Melmed, and E.J. Lavernia: *Metall. Mater.Trans. A*, 2001, vol. 32, pp. 2335-2345.
224. J.E. Burke: Trans.TMS-AIME, 1949, vol. 180, pp. 73-79.
225. A.P. Newbery, S.R. Nutt, and E.J. Lavernia: *JOM*, 2006, vol. 58, pp. 56-61.
226. E. Kuş, Z. Lee, S. Nutt, and F. Mansfeld: *Corrosion*, 2006, vol. 62, pp. 152-154.

Figure Captions.

Fig. 1 OIM images for high purity aluminum in (a) the initial unprocessed condition and after ECAP through (b) 1, (c) 2, (d) 3, (e) 4, (f) 8 and (g) 12 passes using route B_C at RT: the grain colors correspond to the orientations in the unit triangle [44].

Fig. 2 EBSD orientation images of Cu-0.1% Zr disks processed by HPT for (a) 1/4 turn, (b) 5 turns and (c) 10 turns: the columns display images from the center of the disk (on left) and at the edge of the disk (on right) [57].

Fig. 3 Schematic illustration of the principle of the ECAP–Conform process [72].

Fig. 4 Multilayered structure with alternate distribution of finer and coarser grains fabricated by an ABAB-type 5N-Al/4N-Al bimetallic tube with 2 turns of t-HPS at RT: the 4NAl layers have finer grain size(<1 μm) and the 5N Al layers have relatively coarser grains [78].

Fig. 5 Color-coded contour maps of the Vickers microhardness for the Al/Mg system after HPT for 1 turn (upper), 5 turns (center) and 10 turns (lower): the values associated with the various colors are given in the hardness color key on the right [120].

Fig. 6 The range of fracture toughness and strength-to-weight ratio for many metals and materials [128] where the synthesized Al-Mg system shown in Fig. 5 after HPT is incorporated into the diagram as HPT-induced aluminum MMNCs without delineating any upper limits for these values [122].

Fig.7: Model predictions of (a) grain size, and (b) interfacial solute excess for Fe-Zr alloys [147].

Fig. 8: The nanostructure stability map for tungsten-based alloys at 1373 K (1100^{o}C), calculated on the basis of variation of the enthalpy parameters. For each combination of parameters, the free energy of nanocrystalline structures is compared to that of the bulk regular solution. An example for the nanocrystalline stable region in given in (B) for W-Sc. A bulk stable case is given in (C) for W-Ag. (Reproduced with permission from reference [149]).

Fig. 9. Bright field grain size histogram for Fe – 10 at.% Cr – 2 at.% Zr sample annealed at 1173K (900˚C) [154].

Fig. 10. Figure 10. Hall-Petch plot of Fe – 14Cr – 4Hf alloy along with the base Fe – 14Cr alloy [155].

Fig. 11. Model prediction for Fe – 14Cr – x Hf alloys for grain size [156].Fig. 12: Literature data for thermal stabilization mechanisms vs. maximum homologous temperature for stabilization.

Fig. 12. Figure 12. Literature data for thermal stabilization mechanisms vs. maximum homologous temperature for stabilization [156]. The symbols are: thermodynamic stabilization: ●, kinetic stabilization: ○, kinetic and thermodynamic stabilization: ▼, kinetic and complexion stabilization: Δ

Fig. 13: Comparison of the average grain size evolution with milling time for Zn powder milled at room temperature and at liquid nitrogen temperature [179].

Fig. 14: HREM image of Al-7.5Mg alloy cryomilled for 8 h, (a) Image of a whole nanoscale twin. (b) Local magnification of a twin [193].

1288

1289

Article File with Track Changes.

As per the Response Letter, we have not made any changes in the original manuscript.

C. C. Koch, T. G. Langdon, E. J. Lavernia

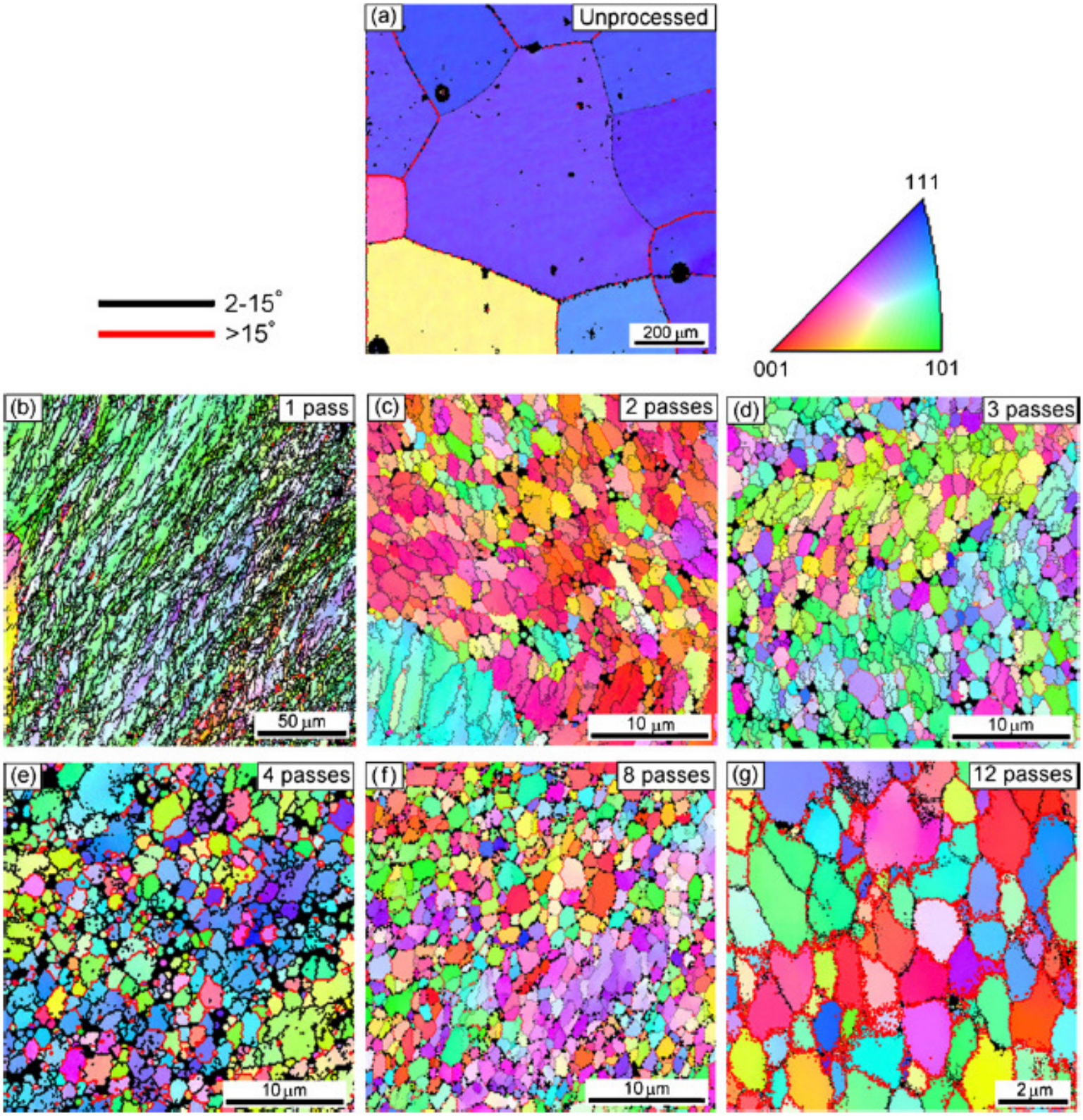
(a)
Unprocessed
200 μm
2-15°
>15°
111
001
101
(b)
1 pass
50 μm
(c)
2 passes
10 μm
(d)
3 passes
10 μm
(e)
4 passes
10 μm
(f)
8 passes
10 μm
(g)
12 passes
2 μm

Cu-0.1 wt.% Zr
HPT: 6.0 GPa, RT

N = 1/4 turn

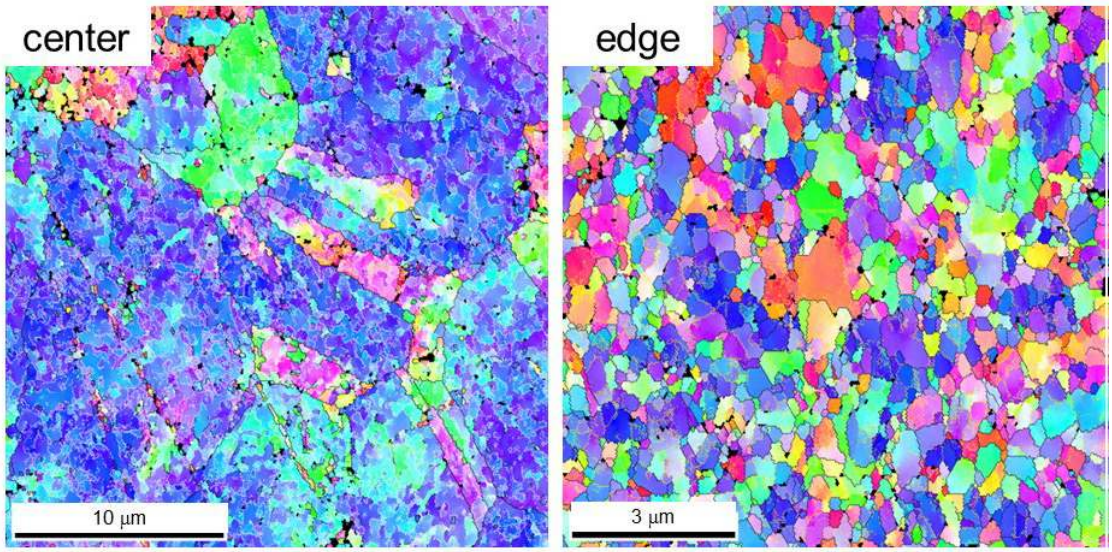

(a)

N = 5 turns

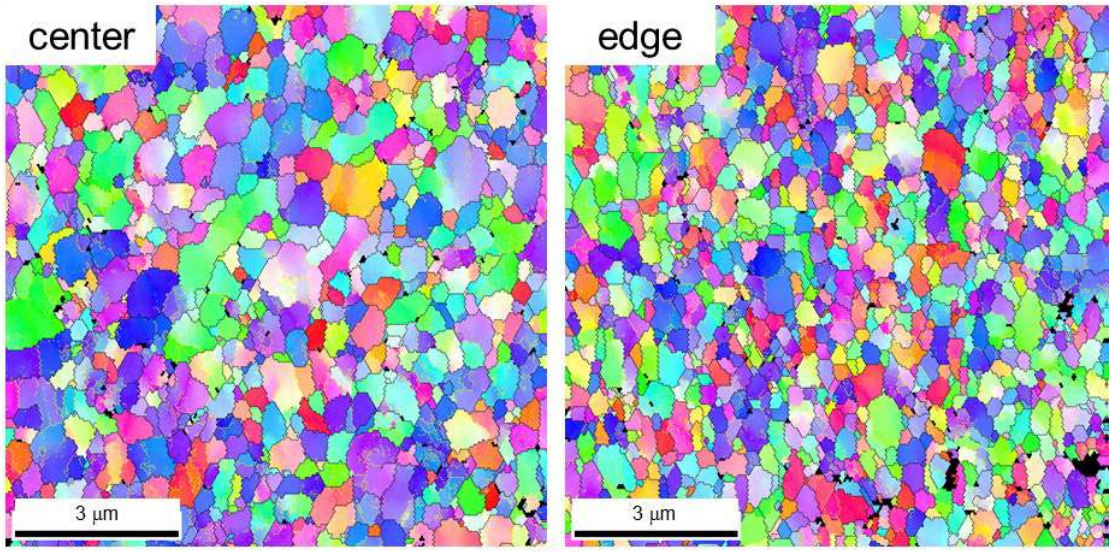

(b)

N = 10 turns

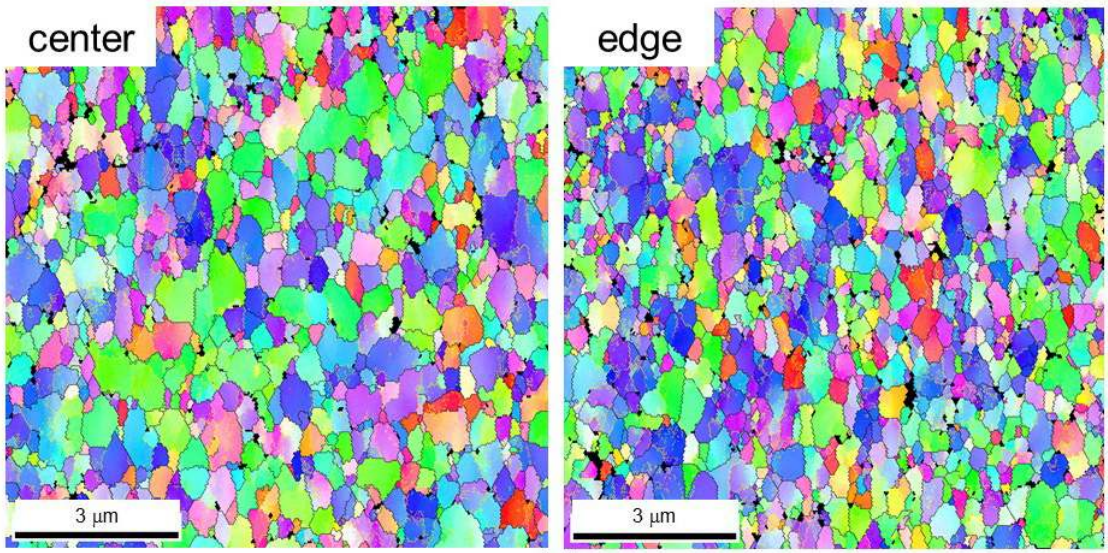

(c)

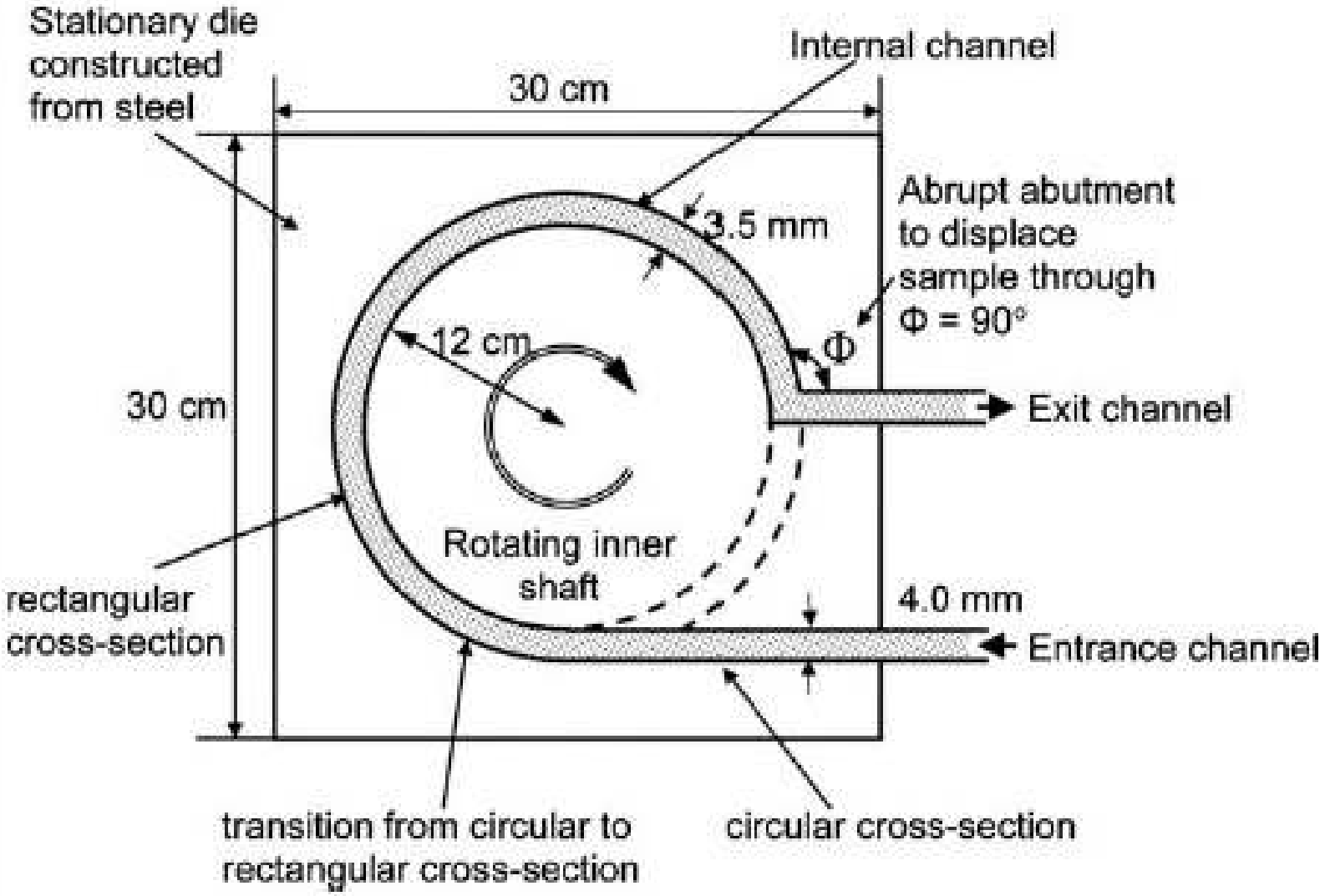
Stationary die constructed from steel
30 cm
Internal channel
3.5 mm
Abrupt abutment to displace sample through Φ = 90°
12 cm
Φ
30 cm
Exit channel
Rotating inner shaft
rectangular cross-section
4.0 mm
Entrance channel
transition from circular to rectangular cross-section
circular cross-section

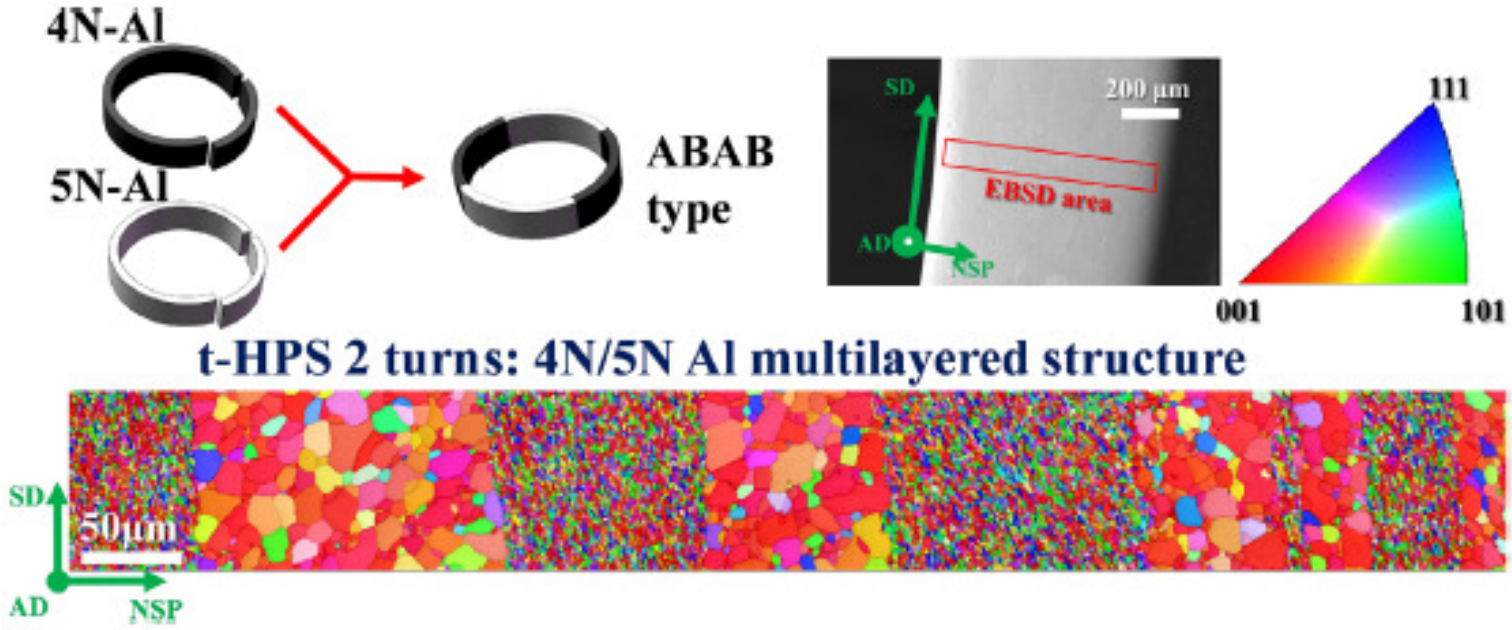
4N-Al
5N-Al
ABAB
type
SD
200 μm
EBSD area
AD
NSP
111
001
101
t-HPS 2 turns: 4N/5N Al multilayered structure
SD
50μm
AD
NSP

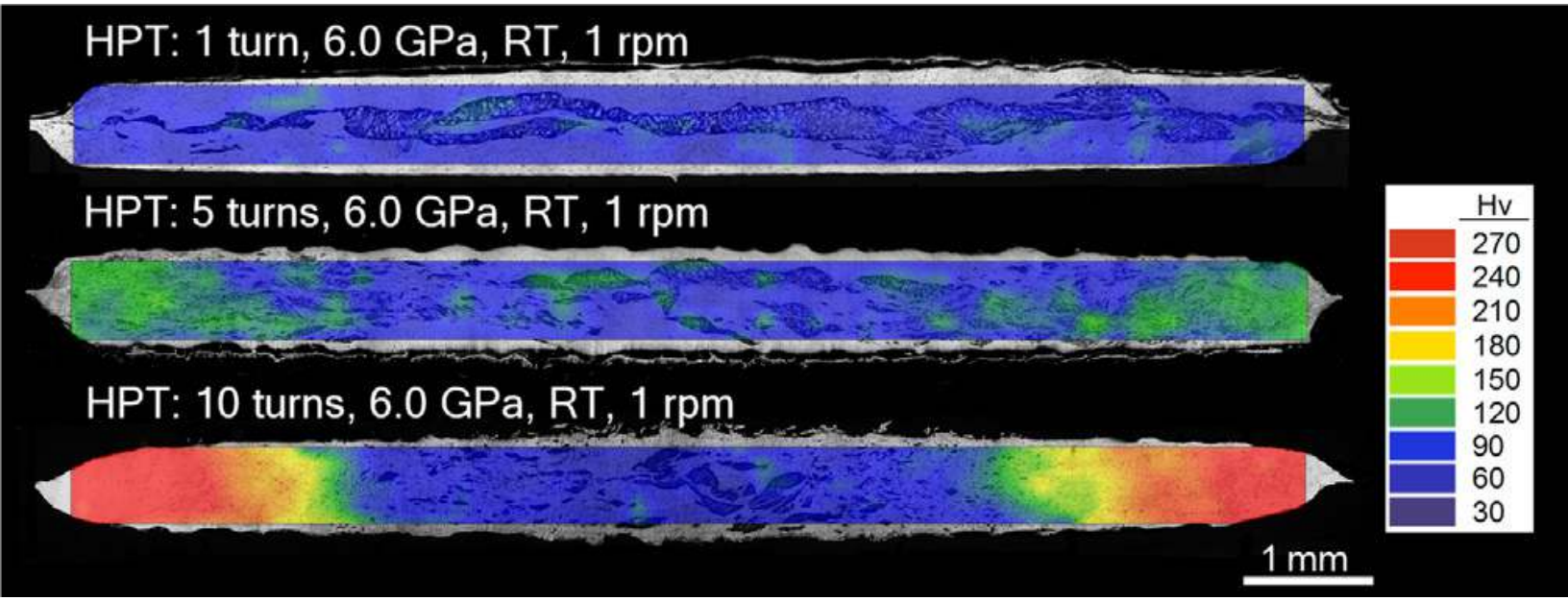
HPT: 1 turn, 6.0 GPa, RT, 1 rpm
HPT: 5 turns, 6.0 GPa, RT, 1 rpm
HPT: 10 turns, 6.0 GPa, RT, 1 rpm
Hv
270
240
210
180
150
120
90
60
30
1 mm

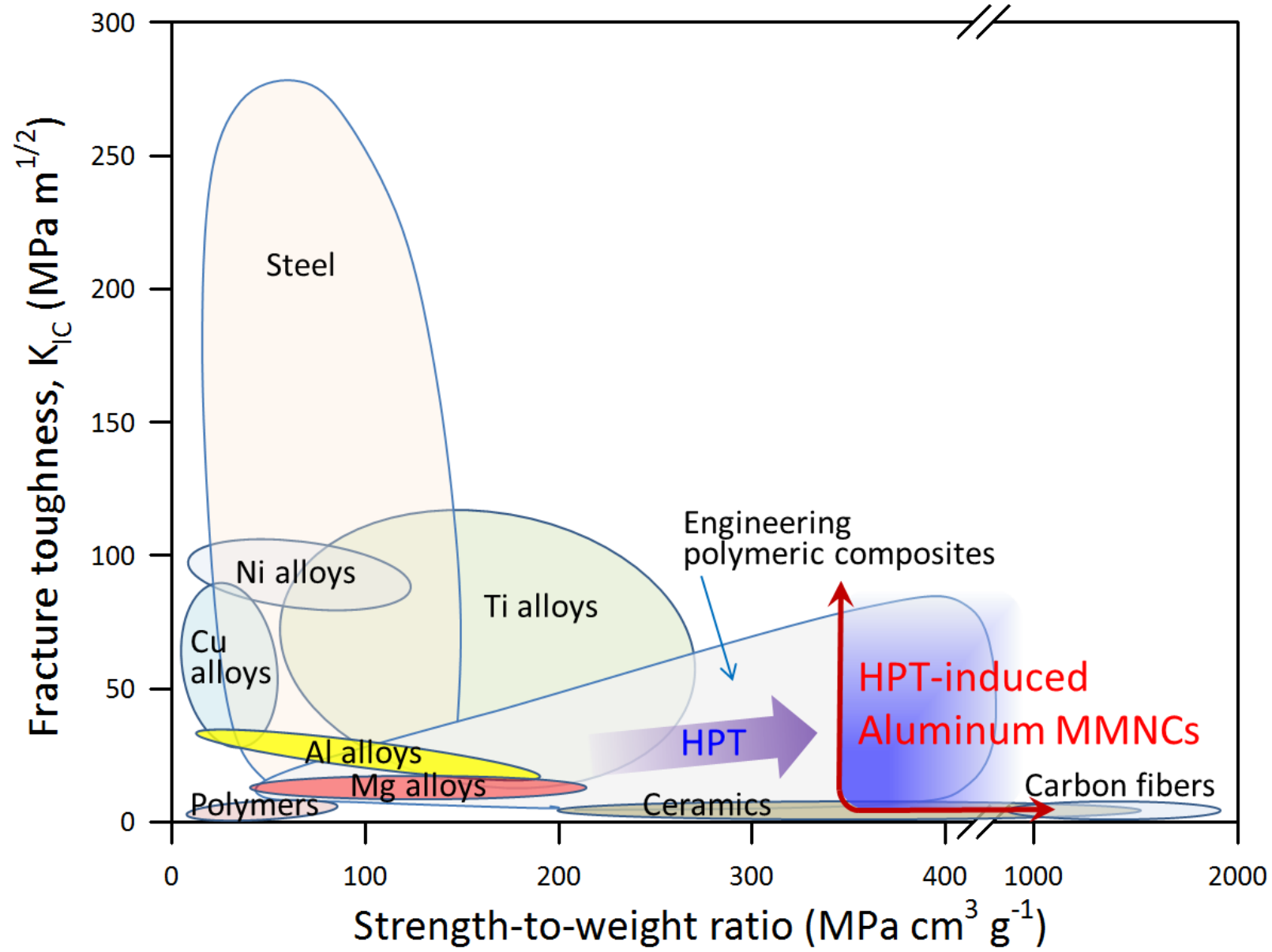
Fracture toughness, K_{IC} (MPa $m^{1/2}$)
300
250
200
150
100
50
0
Steel
Ni alloys
Ti alloys
Cu alloys
Al alloys
Mg alloys
Polymers
Ceramics
Engineering polymeric composites
HPT
HPT-induced Aluminum MMNCs
Carbon fibers
0
100
200
300
400
1000
2000
Strength-to-weight ratio (MPa cm^3 g^{-1})

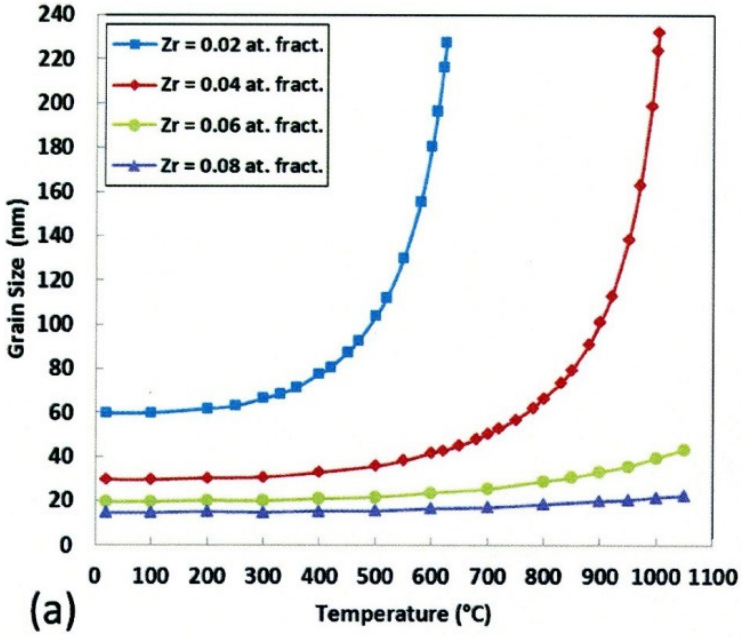
Zr = 0.02 at. fract.
Zr = 0.04 at. fract.
Zr = 0.06 at. fract.
Zr = 0.08 at. fract.
Grain Size (nm)
0
20
40
60
80
100
120
140
160
180
200
220
240
0
100
200
300
400
500
600
700
800
900
1000
1100
Temperature (°C)

(a)

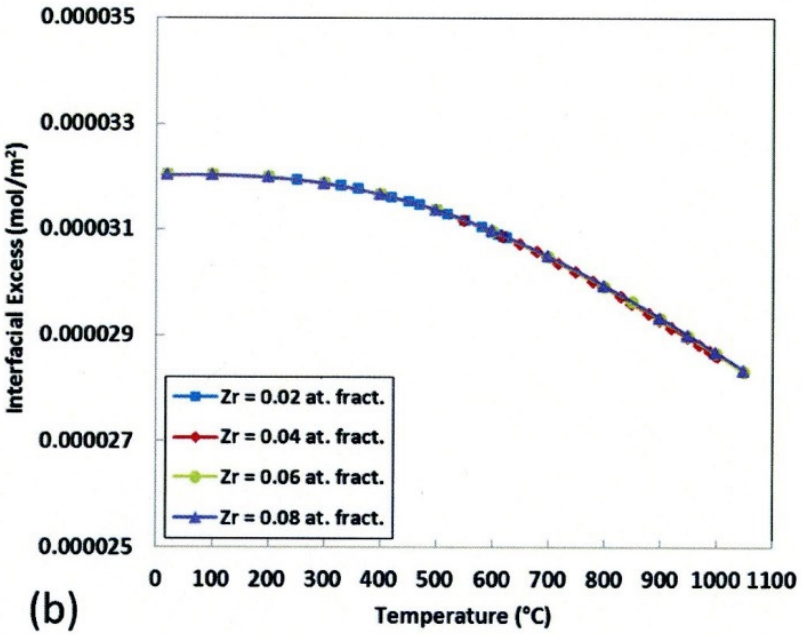
Zr = 0.02 at. fract.
Zr = 0.04 at. fract.
Zr = 0.06 at. fract.
Zr = 0.08 at. fract.
Interfacial Excess (mol/m²)
0.000025
0.000027
0.000029
0.000031
0.000033
0.000035
0
100
200
300
400
500
600
700
800
900
1000
1100
Temperature (°C)

(b)

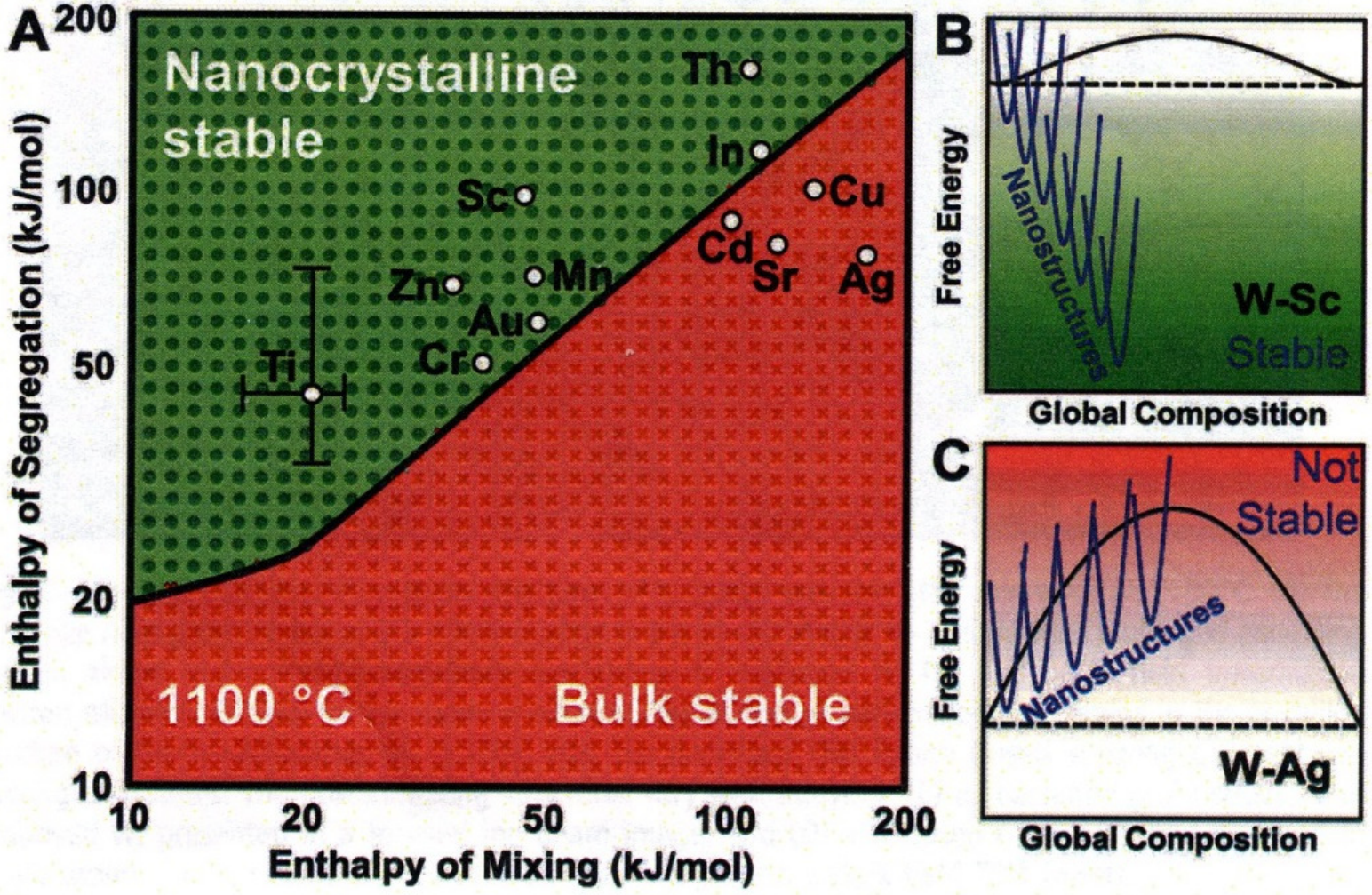
A
200
100
50
20
10
Enthalpy of Segregation (kJ/mol)
Nanocrystalline
stable
1100 °C
Bulk stable
Th
In
Sc
Cu
Cd
Sr
Ag
Zn
Mn
Au
Cr
Ti
10
20
50
100
200
Enthalpy of Mixing (kJ/mol)
B
Free Energy
Nanostructures
W-Sc
Stable
Global Composition
C
Not
Stable
Free Energy
Nanostructures
W-Ag
Global Composition

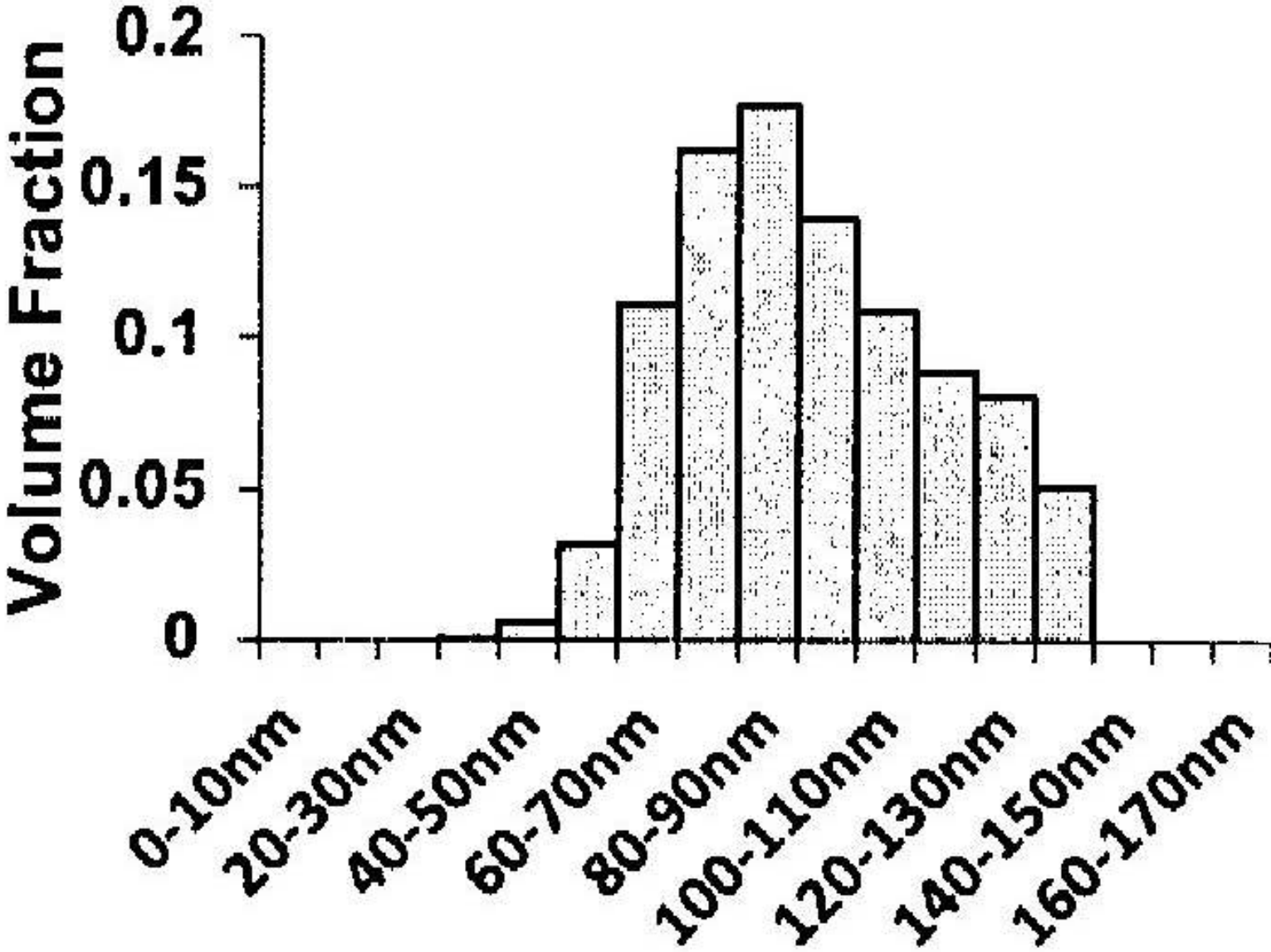
Volume Fraction
0.2
0.15
0.1
0.05
0
0-10nm
20-30nm
40-50nm
60-70nm
80-90nm
100-110nm
120-130nm
140-150nm
160-170nm

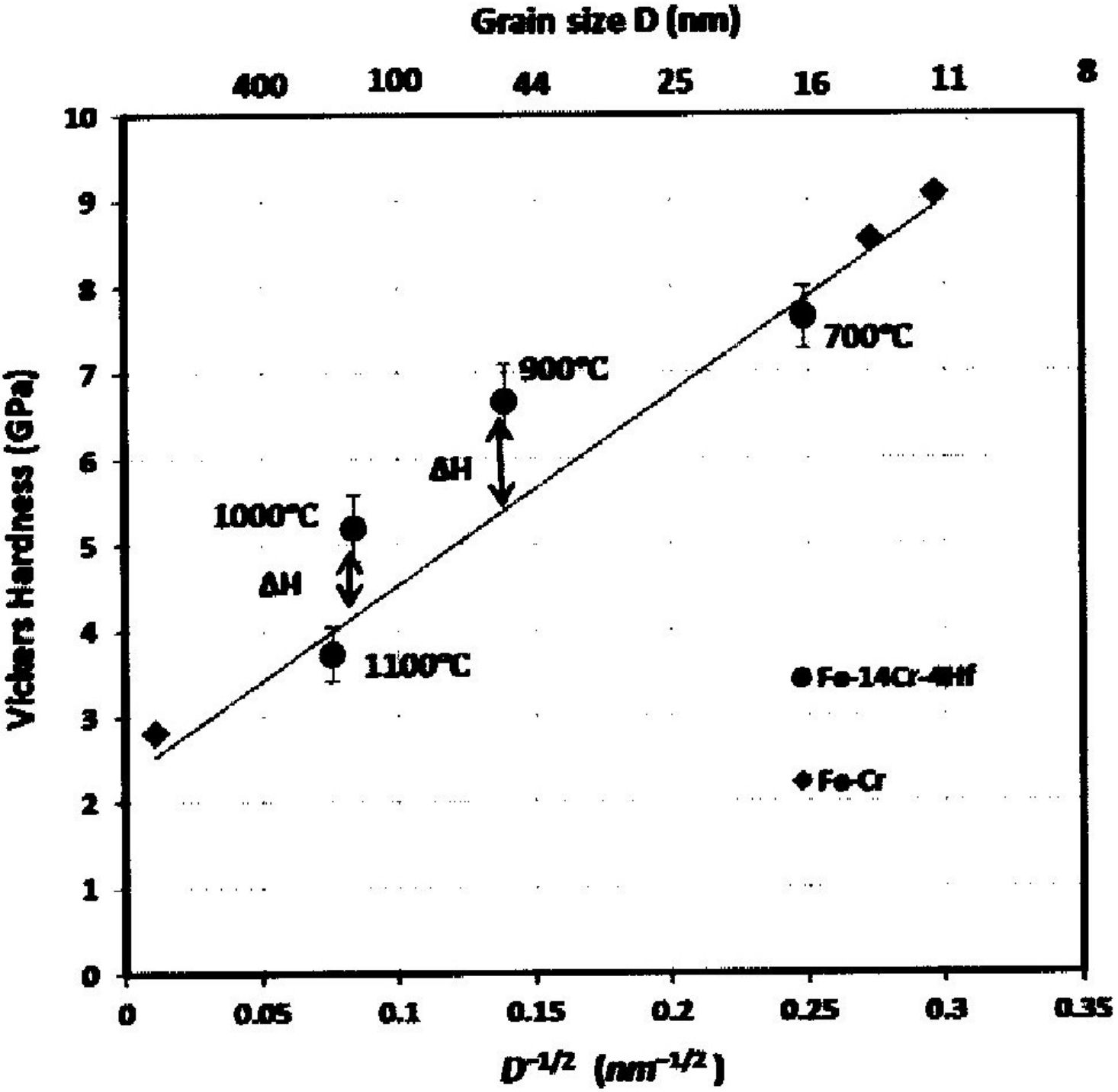
Grain size D (nm)
400
100
44
25
16
11
8
Vickers Hardness (GPa)
10
9
8
7
6
5
4
3
2
1
0
700°C
900°C
ΔH
1000°C
ΔH
1100°C
Fe-14Cr-4Hf
Fe-Cr
0
0.05
0.1
0.15
0.2
0.25
0.3
0.35
D^-1/2 (nm^-1/2)

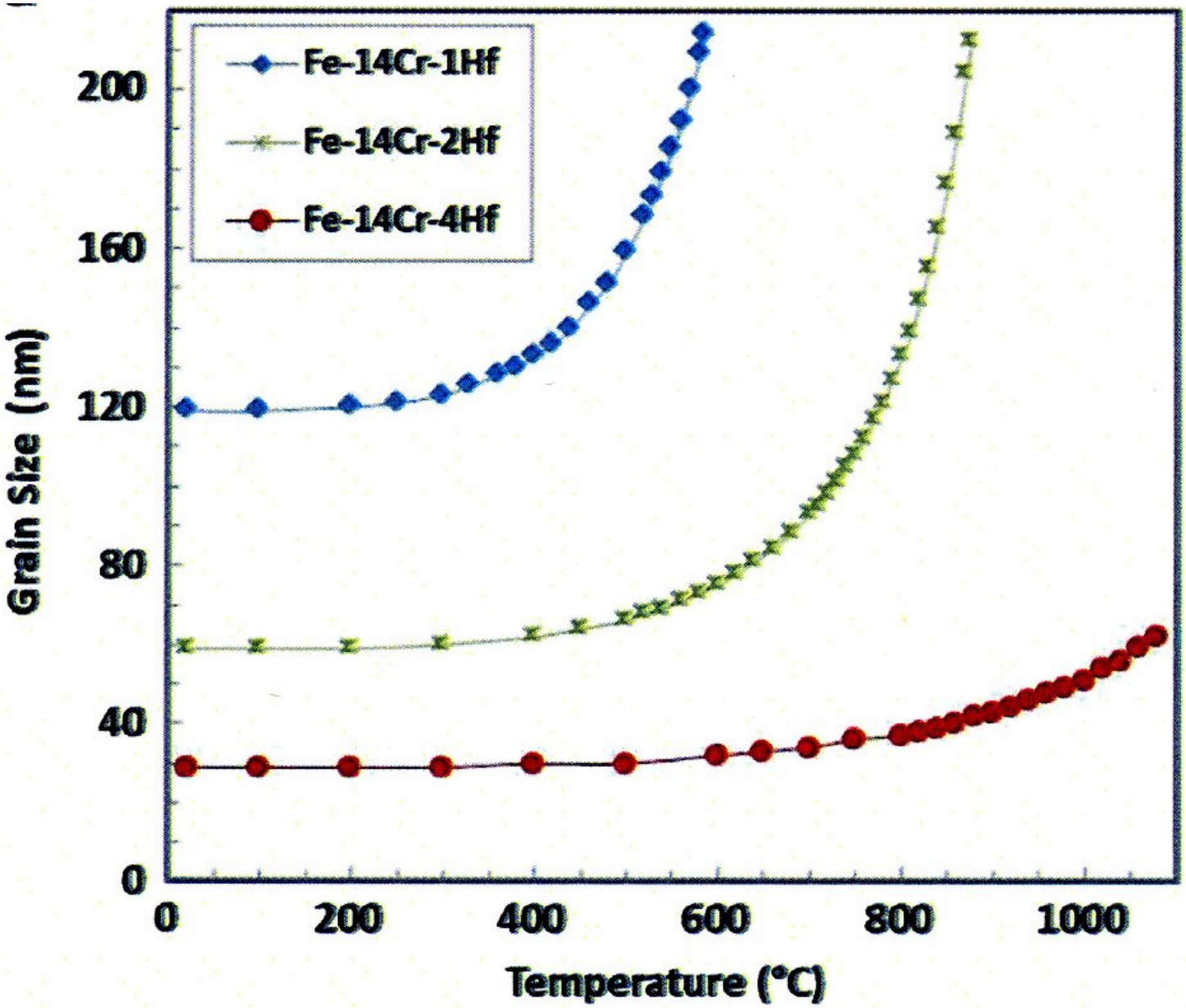
Fe-14Cr-1Hf
Fe-14Cr-2Hf
Fe-14Cr-4Hf
Grain Size (nm)
0
40
80
120
160
200
0
200
400
600
800
1000
Temperature (°C)

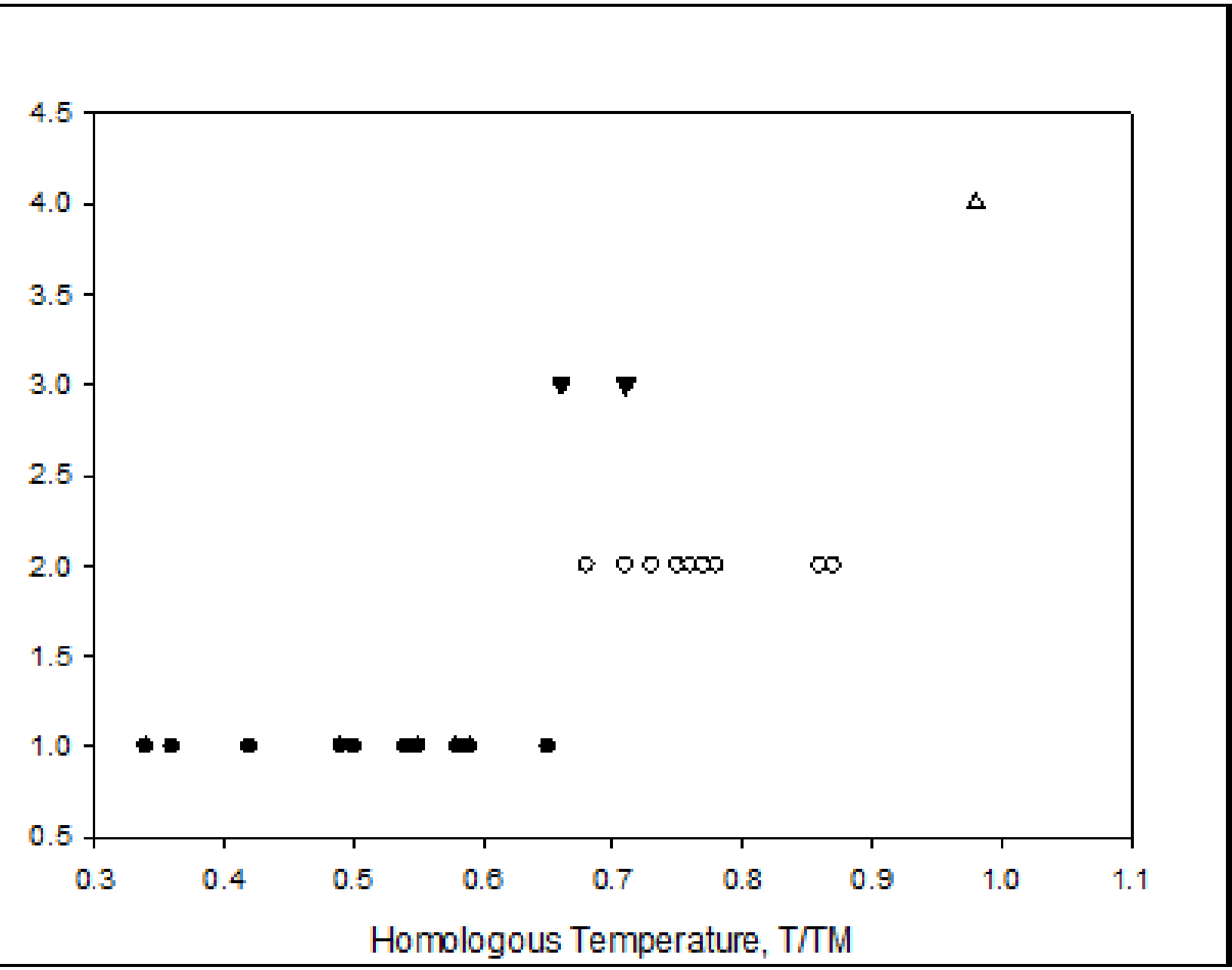
4.5
4.0
3.5
3.0
2.5
2.0
1.5
1.0
0.5
0.3
0.4
0.5
0.6
0.7
0.8
0.9
1.0
1.1
Homologous Temperature, T/TM

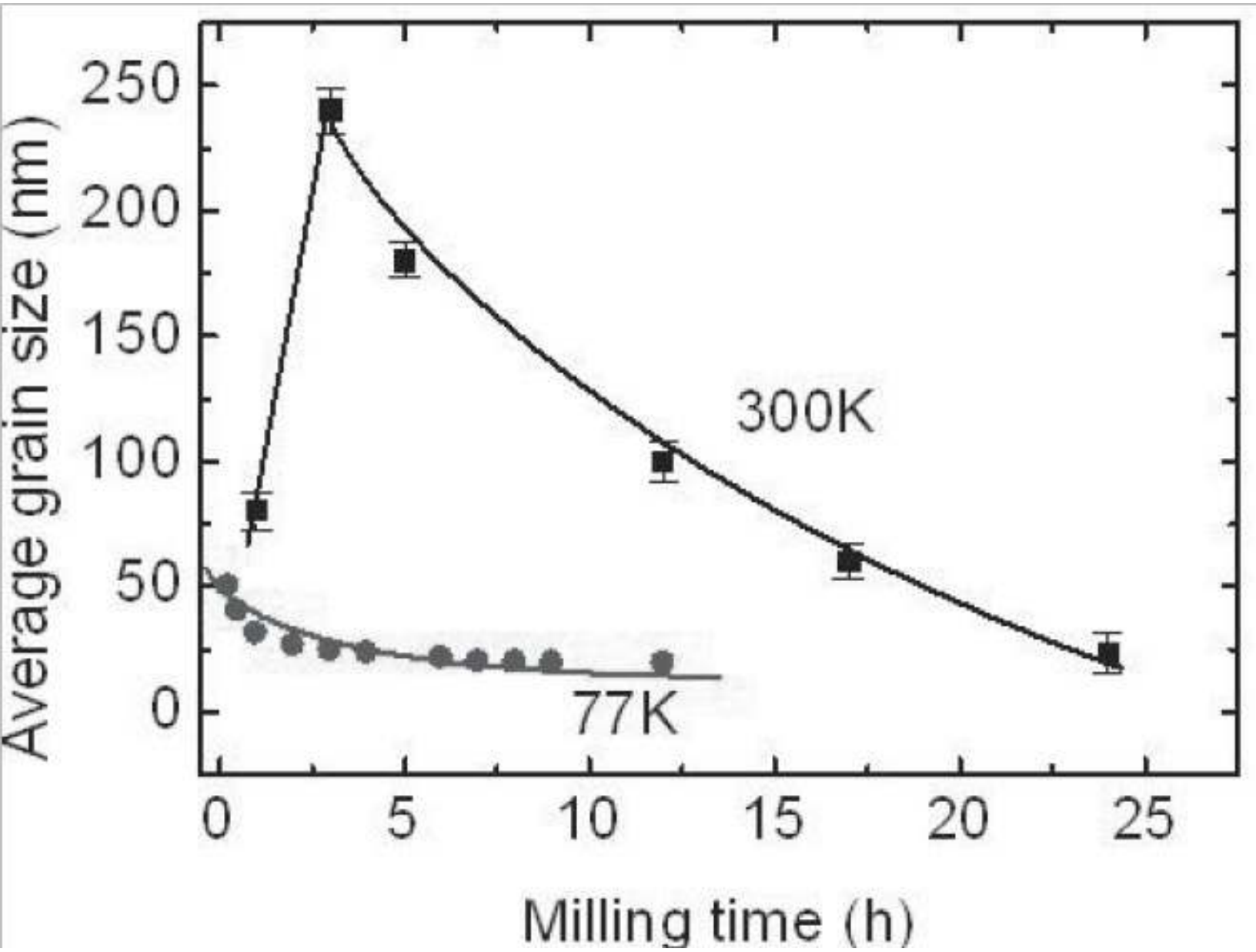
Average grain size (nm)
250
200
150
100
50
0
300K
77K
0
5
10
15
20
25
Milling time (h)

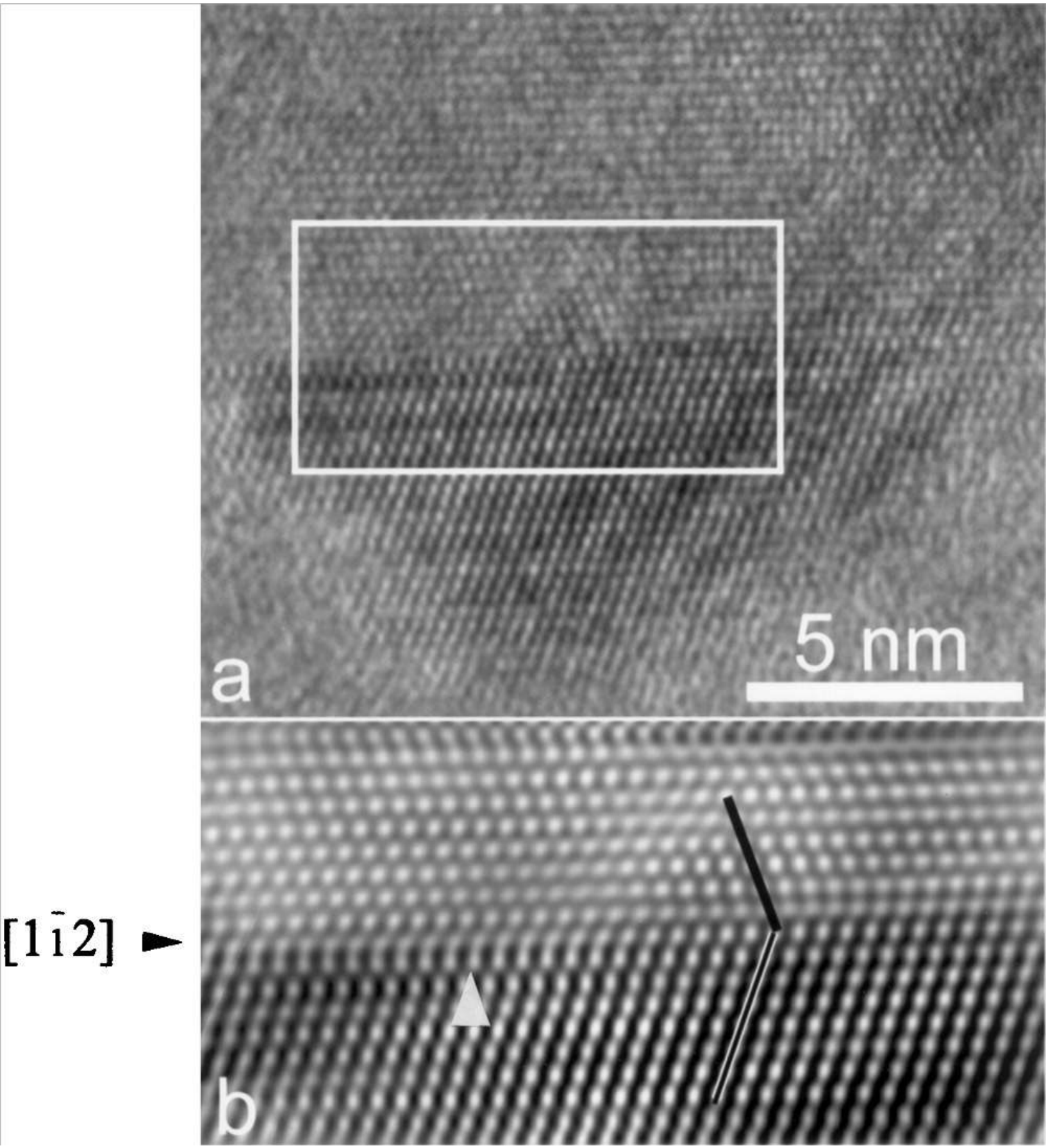
5 nm
a
b
[1$\bar{1}$2]